



An Observational Case Study of a Radiation Fog Event

ARUN GANDHI,¹ ISTVÁN GERESDI,² ANDRÁS ZÉNÓ GYÖNGYÖSI,^{1,3} ÁGOSTON VILMOS TORDAI,¹ PÉTER TORMA,^{4,5}
ANDRÁS REHAK,⁴ MARIANN BÍRÓ-SZILÁGYI,⁴ GYULA HORVATH,⁶ ZITA FERENCZI,⁶ KORNÉLIA IMRE,⁷ ISTVÁN LÁZÁR,⁸
ANDRÁS PETERKA,² and TAMÁS WEIDINGER¹

Abstract—A micrometeorological fog experiment was carried out in Budapest, Hungary during the winter half year of 2020–2021. The field observation involved (i) standard meteorological and radiosonde measurements; (ii) surface radiation balance and energy budget components, and (iii) ceilometer measurements. 23 fog events occurred during the whole campaign. Foggy events were categorized based on two different methods suggested by Tardif and Rasmussen (2007) and Lin et al. (2022). Using the Present Weather Detector and Visibility sensor (PWD12), duration of foggy periods are approximately shorter ($\sim 9\%$) compared to ceilometer measurements. The categorization of fog based on two different methods suggests that duration of radiation fogs is lower

compared to that of cloud base lowering (CBL) fogs. The results of analysis of observed data about the longest fog event suggest that (i) it was a radiation fog that developed from the surface upwards with condition of a near neutral temperature profile. Near the surface the turbulent kinetic energy and turbulent momentum fluxes remained smaller than $0.4 \text{ m}^2 \text{ s}^{-2}$ and $0.06 \text{ kg m}^{-1} \text{ s}^{-2}$, respectively. In the surface layer the vertical profile of the sensible heat flux was near constant (it changes with height $\sim 10\%$), and during the evolution of the fog, its maximum value was smaller than 25 W m^{-2} , (ii) the dissipation of the fog occurred due to increase of turbulence, (iii) longwave energy budget was close to zero during fog, and a significant increase of virtual potential temperature with height was observed before fog onset. The complete dataset gives an opportunity to quantify local effects, such as tracking the effect of strengthening of wind for modification of stability, surface layer profiles and visibility. Fog formation, development and dissipation are quantified based on the micrometeorological observations performed in suburb area of Budapest, providing a processing algorithm for investigating various fog events for synoptic analysis and for optimization of numerical model parameterizations.

Supplementary Information The online version contains supplementary material available at <https://doi.org/10.1007/s00024-024-03498-w>.

¹ Department of Meteorology, Institute of Geography and Earth Sciences, Faculty of Sciences, ELTE Eötvös Loránd University, P.O. Box 32, 1518 Budapest, Hungary. E-mail: arun.elte@gmail.com; arunbestinme@student.elte.hu; andras.zeno.gyongyosi@mouldtech.hu; agoston.contact@gmail.com; weidi@staff.elte.hu

² Institute of Geography and Earth Sciences, Faculty of Sciences, University of Pécs, Ifjúság Street 6, 7624 Pécs, Hungary. E-mail: geresdi@ttk.pte.hu

³ MouldTech Systems Ltd., Fuvar Utca 7, 8900 Zalaegerszeg, Hungary.

⁴ Department of Hydraulic and Water Resources Engineering, National Laboratory for Water Science and Water Security, Faculty of Civil Engineering, Budapest University of Technology and Economics, 3 Műegyetem Rkp., Budapest 1111, Hungary. E-mail: torma.peter@epito.bme.hu; rehak.andras@epito.bme.hu; szilagyimariann@epito.bme.hu

⁵ HUN-REN-SZTE Research Group for Photoacoustic Monitoring of Environmental Processes, Dóm tér 9, 6720 Szeged, Hungary.

⁶ HungaroMet, Budapest, Kitaibel Pál Street 1, 1024 Budapest, Hungary. E-mail: horvath.gy@met.hu; ferenczi.z@met.hu

⁷ HUN-REN-PE Air Chemistry Research Group, University of Pannonia, P.O. Box 158, 8201 Veszprém, Hungary. E-mail: imre.kornelia@mk.uni-pannon.hu

⁸ Department of Meteorology, Institute of Earth Sciences, Faculty of Sciences and Technology, University of Debrecen, Egyetem Square 1, 4032 Debrecen, Hungary. E-mail: lazar.istvan@science.unideb.hu

Keywords: Energy budget components, Fog, Micrometeorology, Turbulent fluxes, Visibility.

1. Introduction

Fog has been a topic of extensive research ever since the beginning of the twentieth century (Möller, 2008). Fog reduces horizontal visibility to less than 1 km due to the suspension of water droplets and ice particles closer to the surface (Gultepe et al., 2007; Klemm & Lin, 2016). This 1 km limit has remained unchanged since the first international conference of the International Meteorological Organization (IMO) in Vienna in 1873 (Houze & Houze, 2019; Gandhi et al., 2022).

The depth and horizontal extent of fog in addition to the synoptic situation depend on the surface

characteristics, micro- and mesoscale meteorological factors, and turbulence near the surface (Gultepe et al., 2007). Fog (especially the radiation type one) is formed under stable boundary layer conditions with low wind speeds and low turbulent intensities under clear skies (Dorman et al., 2021; Meyer & Lala, 1990; Zhou & Ferrier, 2008). Many field experiments have studied the relationship between turbulence and fog formation (Bergot et al., 2007; Duynkerke, 1999; Gultepe et al., 2016; Nakanishi, 2000; Price, 2019; Zhou & Ferrier, 2008), however uncertainties exist regarding the magnitude or threshold value of turbulence intensity that allows fog formation. For example, the near surface vertical wind velocity variance was observed in the range of $0.002\text{--}0.005\text{ m}^2\text{ s}^{-2}$ during the LANFEX fog experiment (Price et al., 2018). The maximum values of the near surface turbulent kinetic energy (*TKE*) which is mostly determined by the wind speed and horizontal wind fluctuations were around $0.4\text{ m}^2\text{ s}^{-2}$ at altitude of 12.5 m during the WiFEX fog experiment in New Delhi (Dhangar et al., 2021).

Microphysical conditions such as droplet number concentration (N_c), effective drop radius (r_d) and liquid water content (*LWC*) are characteristic features of fog. Cooling rate and aerosol concentration significantly impact the characteristics of the fog and its formation. When relative humidity approaches 100%, deliquesced particles promote fog formation by withdrawing the water vapor from the supersaturated air (Price, 2019; Shen et al., 2018). It has also been found that during fog, supersaturation can be of the order of 0.1–0.15% or smaller. However, results of numerical experiments in Budapest gave smaller standard values of not more than 0.01% (Bodaballa et al., 2022). Size of suspended water droplets during fog has been observed to be mostly between 10–20 μm in diameter (Gultepe et al., 2007; Klemm et al., 2005). However, fog instruments provide a possibility to monitor fog particles size up to 50 μm as confirmed by Liu et al. (2020) during dense foggy events in Tianjin, China. This fog particle size diameter is not typical above 30 μm . It is to be noted that during field measurements, the accuracy of the temperature/relative humidity sensors can decrease above 90% (Griesel et al., 2012; Kyrouac & Theisen, 2017). These deviations, hysteresis or drift effects can

also cause issues with response time of the instrument. The difference between saturation vapor pressures above the surface of water and that of ice must also be taken into account (Hang et al., 2016).

One major aspect of fog forecasting is accurate prediction of visibility. Understanding the impact of hygroscopicity, *LWC* and N_c on fog formation is crucial to improve microphysical parametrizations (Bodaballa et al., 2022). Other factors that are crucial in fog forecasting are the proper parametrizations of turbulence, radiation, and aerosol chemistry processes. A wide variety of fog models, ranging from simple 1D models (Bari, 2019; Bergot et al., 2007) to complex 3D models have been applied to regional forecasting of fog events (Pithani et al., 2020; Szintai et al., 2019). Recently machine learning techniques (Lee et al., 2021) and statistical methods, as well as combined numerical and statistical model approaches (Menut et al., 2014; Tuba & Bottyán, 2018) are also being used to improve the numerical weather prediction (NWP). However, 1D models don't consider dynamical processes like horizontal advection and large-scale subsidence (Gultepe, 2008). On the other hand, 3D models have coarser grid resolutions and thus do not resolve the surface patterns with necessary details. Parametrizations of local advection, soil temperature and soil moisture effects in sub-km scales, adapting the cloud parameterization methods for fog formation and coupling of the meteorological and air chemistry models are also unsolved problems (Peterka et al., 2024). Both the 1D and 3D models have deficiencies in forecasting patchy fog patterns. Therefore, these deficiencies are being addressed in many modelling studies around the world (Baklanov et al., 2017; Smith et al., 2021). Szintai et al. (2019) conducted several sensitivity tests and compared NWP simulations for a wintertime low level cloud case (fog) and found that NWP underestimated cloud cover. Kumar and Schmeller (2022) investigated a wintertime fog event using WRF simulation and validation using surface observations. They found significant bias between observations and simulations with PBL schemes significantly influencing the fog durations.

To improve our knowledge about the life cycle of fog, several comprehensive fog experiments, and international scientific collaborations, including fine

resolution micrometeorological and air chemistry measurements, have been carried out around the world namely European Action COST-722 (Jacobs et al., 2008), ParisFog (Haeffelin et al., 2010), FRAM (Gultepe et al., 2014), MATERHORN-fog experiment in US Utah (Gultepe et al., 2016; Hang et al., 2016), WiFEX (Dhangar et al., 2021; Ghude et al., 2017), LANFEX (Price et al., 2018), Namib Fog Life Cycle Analysis (NaFoLiCA) (Spirig et al., 2019), and C-Fog (Fernando et al., 2021).

The results of ParisFog experiment reveal that turbulent coupling between the surface and the cloud base is responsible for visibility reduction (Haeffelin et al., 2010). Furthermore, sedimentation of droplets along with large scale synoptic situations were found to be significant for fog dissipation. During the Mountain Terrain Atmospheric Modeling and Observations (MATERHORN) campaign, especially the ice fog formation in the high mountain region of Utah, US was studied, and the observation data was compared with the results of WRF mesoscale model (Pu et al., 2016). In the WiFEX experiment (Ghude et al., 2017), authors found that increasing values of potential temperature with height (stable stratification) 2–3 h before fog onset could improve the prediction of foggy situations. In the C-Fog experiment (Fernando et al., 2021), authors concluded that large scale weather systems were not good indicators for fog genesis and evolution, and rather the micrometeorological phenomenon and aerosol dynamics influence fog lifecycle. In the Namibian Coastal fog experiment (NaFoliCA) (Spirig et al., 2019), increase of relative humidity (reaching saturation) due to surface radiative cooling was detected. Radiosonde measurements indicated the presence of stable boundary layer (low wind speeds) at night. During the LANFEX experiment (Price et al., 2018), authors did not find a direct correlation between higher cooling rates occur during evening and fog formation. The cooling rates were directly related to the orography of the valley. The descent of air in steeper or narrower valleys resulted in the highest cooling rates. However, the fog occurrence frequency was moderate in these cases, whereas highest fog events occurred in the widest and shallowest valley. A complex set of micrometeorological instruments was installed to study fog evolution. Although

variability of the characteristics of fog is different, specific results were obtained in these studies. For instance, the high relative humidity (reaching near the saturation), the colder temperature inversion near the surface before fog formation, the development of stable boundary layer, the low wind speeds and turbulence before fog formation are common features of all the fog events observed in the current study experiments conducted. All these fog experiments have used a complex set of micrometeorological instruments to study fog evolution. Many of these fog experiments are being conducted in urban areas despite the impact urban fog can have for instance, road and air traffic delay (Ghude et al., 2017).

A numerical modelling study was performed to validate model results and to understand CCN (cloud condensation nuclei) activation mechanism in the fog (Peterka et al., 2024) and compare modelling results with Hungarian observations (Weidinger et al., 2021a). It is also important to note that this numerical fog experiment was not specifically performed in an urban area rather in the countryside.

Mist and fog occur regularly in the Carpathian Basin (Cséplő et al., 2019) during the winter half-year, affecting also urban. In many places (e.g., at airports, meteorological stations) standard meteorological measurements are being conducted along with surface layer turbulence, energy budget components and boundary layer measurements with remote sensing tools (ceilometer, SODAR/RASS etc.). However, quantification of fog events that occurred in the Carpathian Basin using standard meteorological measurements, ceilometer data, surface layer profile and energy budget measurements have not been performed together. Therefore, field campaigns to improve our knowledge about the environmental conditions that promote fog formation were performed in winter half years from 2018 to 2021 at the suburban area of Budapest. To the best of our knowledge, this was the first comprehensive fog campaign in the Carpathian Basin (Cséplő et al., 2019; Imre et al., 2019; Weidinger et al., 2021a, 2021b). However, there are current projects aimed to study some physical aspects of the fog: (i) using satellite data, meteorological data observed at the surface and topographic information. Pauli et al. (2020) determined the occurrence of fog and

low stratus in Continental Central Europe. (ii) Hůnová et al. (2021) analysed the long-term records about the daily fog events recorded in Romania to study the trend and the seasonal component of the probability of fog occurrence based on different environments and geographical areas. (iii) Several countries in the Carpathian-region participate in the ICOS project. The meteorological stations operating within ICOS are also used to study fog events (Kivalov et al., 2023). (iv) Ovesnik et al. (2012), Matus et al. (2020) and Miclea et al. (2020) published results about the improvement of sensors for detection of fog formation and density.

The main objectives of the paper are as follows: (i) description and quantification of main features of fog events detected during the winter half year of 2020–2021, (ii) building on the data collected by Weidinger et al. (2021a), establishing relationship between fog lifecycle and time evolution of meteorological parameters, surface radiation, energy budget components, and dew formation, (iii) quantification of micrometeorological variables and local effects detected during the longest observed radiation fog event. (iv) preparing case studies that can be further evaluated using NWP model and compared with observations.

2. Instrumentation, Methods and Data Set Description

The observations were performed at the main observatory station of the HungaroMet (former Hungarian Meteorological Service) located at 47.4292 N and 19.1818 E in Pestszentlőrinc (WMO station code—12,843, 139 m alt.), a suburb area of the capital city Budapest, Hungary. The instruments (Fig. 1a and see also Fig. 4) located far from buildings and high vegetation (20–50 m, depending on the direction) are as follows: (i) synoptic meteorological station to measure temperature (T), relative humidity (Rh), wind speed (V) and direction (Dir) at altitude of 10 m (Fig. 1b), pressure (p), visibility (Vis), precipitation ($Precip$) with time resolution of 10 min.; (ii) radiosonde (measurement occurs at 00 and 12 UTC); (iii) instruments for observation of radiation balance components, soil and surface energy budget

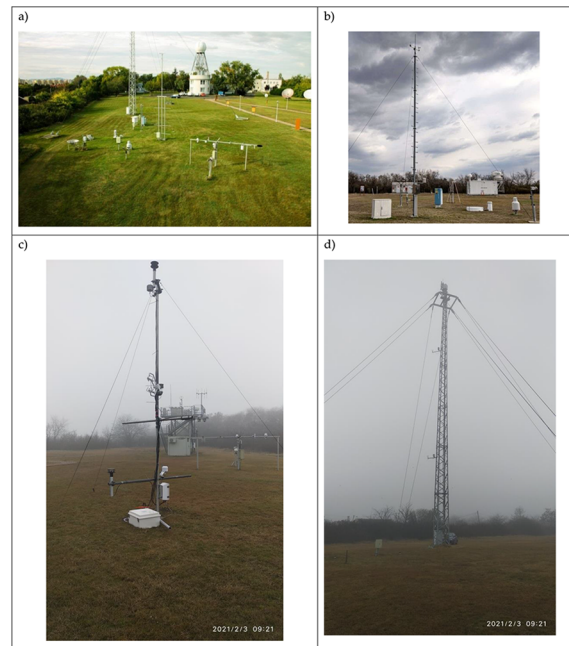


Figure 1

Meteorological garden of the HungaroMet in Budapest, Pestszentlőrinc **a** the locations of surrounding buildings, trees and the 30-m tower, **b** 10-m meteorological pole for standard wind measurement, Lufft CHM 15 k ceilometer and the automatic Vaisala radiosonde container in the background, **c** 5-m micrometeorological pole with 2D sonic anemometers, temperature/relative humidity sensors with Campbell radiation shelter, CNR1 net radiometer, and the eddy covariance system (CSAT-3 + EC150), **d** 30-m meteorological tower to evaluate temperature (T), relative humidity (Rh) and wind speed (V) profiles and eddy covariances (Gill Solent Windmaster on 30-m)

components with eddy covariance methodology (Fig. 1d); (iv) measurements to estimate the profiles for T , Rh and V at altitudes of 5 m (Fig. 1c) and 30 m (see tower in Fig. 1d). Eddy covariance for calculating the fluxes were evaluated by the measurements at the altitudes of 2.5 m and 30 m with 10 Hz time resolution; (v) Lufft CHM 15 k ceilometer (Fig. 1b) to detect fog formation and dissipation. Data generated by micrometeorological measurements were collected using Campbell CR1000 and CR3000 dataloggers, and with a microcomputer for the Gill Solent Windmaster 3D sonic anemometer. Sensor types, heights, averaging times, and measuring periods are provided in Tables 1 and 2.

Standard meteorological measurements were used from the 1st of October 2020 to the 31st of March 2021. Visibility and present weather conditions were

Table 1

Instruments installed on the 5-m meteorological pole

Instrument	Height(s)	Variables	Resolution
Campbell Scientific CSAT-3 + EC150*	2.5 m	u, v, w [ms^{-1}], T_s [$^{\circ}\text{C}$], ρ_v [gm^{-3}], c_{CO_2} [ppm], T_{ref} [$^{\circ}\text{C}$], p [hPa] turbulent fluxes: τ [$\text{kgm}^{-1}\text{s}^{-2}$], H, LE [Wm^{-2}], F_{CO_2} [ppmms $^{-1}$]	10 Hz, 30 min (for fluxes)
Gill 2D Windsonic	1 m, 5 m	wind speed (V [ms^{-1}]) and direction (Dir [degree, $^{\circ}$])	1 min
Campbell Scientific HMP60-ET	1 m, 5 m	T [$^{\circ}\text{C}$], Rh [%]	1 min
Kipp & Zonen CNR1**	2 m	Radiation balance components: shortwave ($G_s \downarrow, G_s \uparrow$), longwave ($G_l \downarrow, G_l \uparrow$) [Wm^{-2}] and surface temperature [$^{\circ}\text{C}$]	1 min
Campbell Scientific 237 Leaf-Wetness Sensor	0 m	Leaf wetness (Lw [$\text{k}\Omega$]), leaf wetness index (0 – 7999 [-]) and normalized index (0 – 1 [-])	1 min
Campbell Scientific T107	-2, -5, -10 cm	T_{soil} [$^{\circ}\text{C}$] (Soil temperature)	1 min
Campbell Scientific CS616	-2, -5 cm	VWC [%] (volumetric water content)	1 min
Hukseflux HFP01SC/self-calibrated	-8 cm (2 sensors)	G_{soil} [Wm^{-2}] heat flux into the deeper soil	1 min

* u, v, w : wind vector components in the cartesian coordinate system: x – East, y – North and z – vertical direction; T_s : sonic temperature; ρ_v : water vapour density; c_{CO_2} : carbon-dioxide concentration; $\tau, H, LE, F_{\text{CO}_2}$: momentum, sensible and latent heat and CO_2 flux, respectively

** $G_s \downarrow, G_s \uparrow$: incoming solar (or global) radiation and reflex (shortwave) radiation, respectively; $G_l \downarrow, G_l \uparrow$: incoming and outgoing longwave radiation. (Micrometeorological data was collected in the time period from the 21st of November to the 2nd of December 2020 and from the 29th of December 2020 to the 31st of March 2021.). The data between 2nd December 2020 and 28th December was not available due to the malfunctioning of the data logger due to power challenges (S3)

Table 2

Instruments installed on the 30-m meteorological tower

Instrument	Height	Variables	Resolution
Gill Solent		Windmaster 3D u, v, w [ms^{-1}], T_s [$^{\circ}\text{C}$] turbulent fluxes: τ [$\text{kgm}^{-1}\text{s}^{-2}$], H [Wm^{-2}]	30 m 10 Hz 30 min (for fluxes)
Vaisala HMP45C	9 m,	23 m	
T [$^{\circ}\text{C}$], Rh [%]	10 s		
Vaisala WA15		anemometer	9 m, 23 m
wind speed (V [ms^{-1}])	10 s		

(Measuring period was from 21st of November to 31st March 2021, permanently.)

detected using the Vaisala Present Weather Detector and Visibility Sensor (PWD12) by the HungaroMet

placed at 2 m above ground level (AGL). It provides visibility data (Vis) in meters [m] and an estimation data about the accumulated precipitation ($Precip$) in millimeters with ten-minute time resolution.

The Lufft CHM 15 k ceilometer from the HungaroMet is a laser based remote sensing device which actively scans the layers of particles and droplets in the atmosphere (Fig. 1b). It uses the Sky Condition Algorithm (SCA) to compute cloud base and cloud penetration depths, Sky Condition Index (SCI), and additional characteristics of sky conditions (cloudiness, rain, snow, and fog). As per the manual, up to three different aerosol layers are detected. The technique is based on an aerosol layer detection algorithm which itself is based on a wavelet algorithm that identified three different aerosol layers. The identified aerosol layers (height) strongly depend on the local conditions and time. The quality of the height of the identified aerosol layer height is described by Q ,

quality index. This index involves 6 options, values out of which 4 of the options (assigned by numbers of -1 , -2 , -3 and 0) denote that no aerosol layer was not detected, while the other 2 options (assigned by numbers of 1 and 9) show denote that aerosol layer was detected. A value of number 1 means that the layer can be detected with low spatial accuracy, whereas number 9 indicates that aerosol layer can be detected with high spatial accuracy (less than 50 m).

Haze and precipitation are detected and evaluated by multiple scattering and using the SCA algorithm. We used the range corrected backscatter signal from the output of the instrument as suggested by Kolláth and Kolláth (2020) following the manufacturer's documentation (CHM 15 k Manual by Luft 2019).

The radiosonde data (Budapest, 12843) available on the University of Wyoming website was also used (Description of Sounding Columns, University of Wyoming, 2022).

Methodology of the Quality Control and Quality Assessment (QC/QA) of the standard meteorological measurements especially for temperature, relative humidity, and surface energy budget components as well as the turbulent flux calculations are presented in the Supplementary material (S1). The uncertainties and recalibration of the traditional capacity type relative humidity sensors are also presented there.

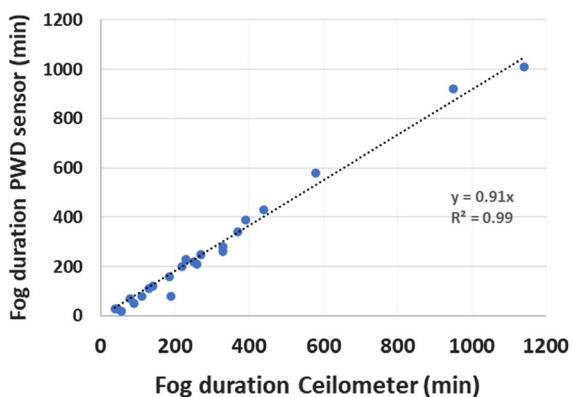


Figure 2
Fog durations (minutes) identified using PWD12 sensor and ceilometer

3. Results and Discussion

3.1. Fog Identification

The foggy periods were identified by using both 10-min averaged visibility and SCI data. Table S3 in the supplementary material (S2) summarizes the foggy periods which were identified by these two sensors. Figure 2 shows that the PWD12 sensor in most of the cases provide smaller values of foggy events approximately by 9% as compared to the ceilometer with correlation coefficient larger than 0.99 . Further we could not decide which instrument is more accurate, since their measurement strategy is different, and so we did not settle on a reference name. We determined the difference and indicated that the current time sensor at 2 m levels in most cases provide a shorter period of foggy event than the ceilometer, which is a more characteristic of the boundary layer.

The PWD12 sensor indicates slightly later onset and earlier dissipation of fog compared to SCI data (Table S2). The duration of fog indicated by the PWD12 is about 0.5 – 1.0 h shorter than that indicated by the ceilometer in few fog events. This discrepancy must be the consequence of the different ways of their operation. PWD12 visibility sensor is placed at 2 m above the surface, and it measures visibility using forward scatter measurement, and the light beam emitted horizontally is scattered by the particles and the forward scattered radiation is detected by the instrument. On the other hand, ceilometer measures the vertical profile of the fog. It observes the backscattering due to droplets. The sampling volume of PWD12 is significantly smaller and it can detect fog only when it occurs at the surface. Furthermore, the spatial variability of the droplets can be significantly different in horizontal and vertical direction.

We classified the detected fog events using the methods suggested by Tardif and Rasmussen (2007) (here after TR2007) and by Lin et al. (2022). The method suggested by TR2007 primarily separates fog into categories of advection, radiation, evaporation, precipitation, and cloud base lowering fog (CBL). CBL fogs form due to the lowering of the base of a low level—stratus cloud. TR2007 suggested using the near surface measurements of wind speed, horizontal

visibility, temperature, precipitation data as well as cloud base heights to identify and categorize different types of foggy events. (See also the climatological study for foggy events detected at Zagreb Airport, Croatia (Zoldos & Jurkovic, 2016)). The method suggested by Lin et al. (2022) is based on modified Richardson number (MRi) and on the cloud base height prior to the fog formation. This index was suggested by the authors to describe the turbulent mixing and dynamic stability of the near surface layer. Using the indexes calculated 3 h before the fog (MRi_{prefog}) and during the fog (MRi_{fog}), fogs are classified into advection, radiation, evaporation, and advection-radiation fog. This method detects CBL fogs if mean cloud base height 3 h before fog onset was less than 1500 m. Therefore, no further calculation of MRi is required in case of CBL fogs (Tables 4 and 5 in supplementary material S3). The fog classifications evaluated by both methods along with the average, maximum and minimum observed visibilities. Using the TR2007 method 15 radiation fogs and 8 CBL fogs were detected. The second method categorizes 11 fogs into radiation fog category, 8 fogs into CBL fog category and 4 fog events could not be classified by this method. The reason why both methods do/did not agree for the radiation fog is that the nature of calculation of modified local bulk Richardson number based on surface temperature from well calibrated CNR1 net radiometer. The fog density and thickness are influenced by local effects and surroundings. Therefore, this local method depends on local variables and gives possibility of other type of fog detection at any other location.

Advection fog was not detected by any of these methods, because 5 h prior to onset of the fog the average wind speed near the surface was less than 2.5 m s^{-1} in all the detected fog events. The method suggested by TR2007 requires mean cloud base height less than 1000 m, 5 h prior to fog onset to be classified as CBL fog. Relative Root Mean Square Error ($rRMSE$) values calculated by using the fog duration data obtained from ceilometer and PWD12 sensor reveal higher uncertainty of fog duration in the case of radiation fog category than in the case of CBL fog category. $rRMSE$ values for radiation fog

category and CBL fog category was 15.9% and 13.6%, respectively.

The analysis of the observed cloud base data during the foggy periods reveals that the cloud base height varied between 20 to 80 m. The ceilometer cannot detect any particles which were under the altitude of 15 m. So, if cloud base is detected at 20 m, it does not exclude the possibility that the cloud (fog) can extend closer to the surface. Due to this deficiency ceilometer can miss thin fogs of less than 20 m.

The PWD12 sensor and the ceilometer detected 23 foggy periods (in common) in the time period from October 1st 00:00 UTC to March 31st 23:50 UTC. The highest number of foggy periods (9 in total) were reported in November followed by December and February with four fog events. Only 3 fog events were identified in January. The remaining three fog events occurred in October. The longest continuous foggy period (as per ceilometer data) was detected on 24th November. It formed early morning at 03:30 UTC and dissipated only at 22:30 UTC, lasting for more than 19 h (Table S4). The second longest continuous foggy period started on 2nd February at 17:40 UTC and ended on 3rd February at 09:30 UTC, lasting for about 15:50 h. It was a CBL type fog event.

Figure 2a, c in the supplementary material S4 (Foggy periods along with visibility and relative humidity patterns during the winter half year (1st of October 2020–31st of March 2021)) depicts the time evolution of relative humidity observed at the altitude of 2 m from standard meteorological measurement in HungaroMet (12843) and that of the visibility and precipitation type detected by the PWD12 sensor (see also the Fig. 3 in the supplementary material, S4 for the four longest fog events). The relative humidity is larger than 98% both before the onset and after the dissipation of the fog. Figure 2b, d in the supplementary material S4 depicts the patterns of 1-min averaged relative humidity observed at altitudes of 1 and 23 m. Furthermore, the pattern of the precipitation types indicated by the SCI is also plotted in these panels.

PWD12 sensor detected precipitation 2 to 3 h before or after the fog events in few cases (4 times). Spirig et al. (2019) found that the accumulated

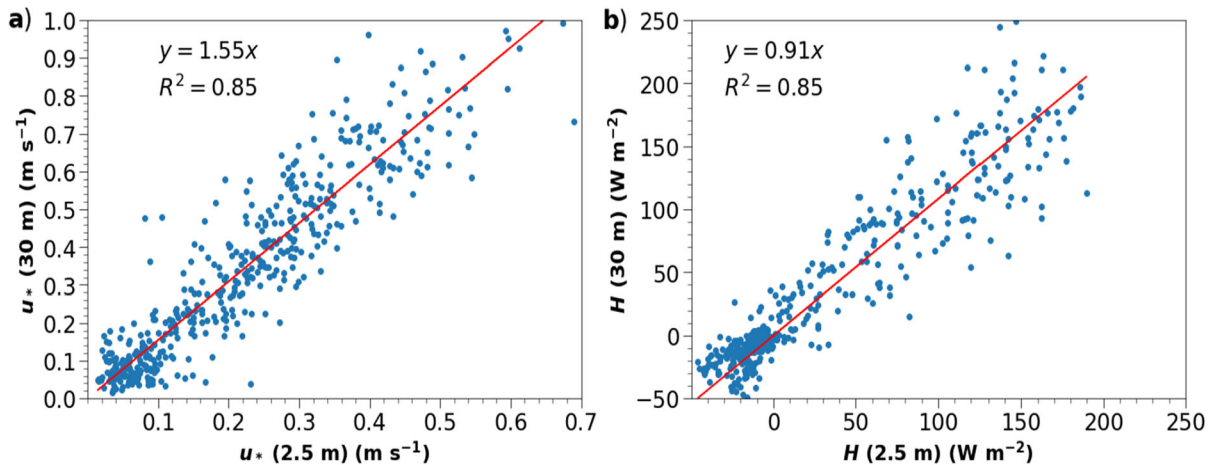


Figure 3

Relation between **a** friction velocities (u_*) and **b** sensible heat fluxes (H) observed at altitudes of 2.5 m and 30 m during the whole measurement campaign in 2020–2021. The red line in the panels is the regression line

precipitation related to a foggy event can be more than 6 mm. However, the accumulated precipitations observed by PWD12 sensor did not exceed 0.2 mm in any case. Feigenwinter et al. (2020) reported that sampling the precipitation by microlysimeters, the accumulated precipitation formed due to the settling of the fog droplets varied between 0.2 to 0.9 mm.

The ceilometer SCI index reports rain before and after foggy events more frequently because of the sedimentation of the fog drops (Fig. 2b, d). But this rain is not quantified by the SCI index. Because of this misinterpretation of the precipitation by the ceilometer, the accumulated precipitation observed by PWD12 sensor is more reasonable.

Relative humidity observed at altitudes of 1 m and 23 m are larger than 95% during all the foggy events (Fig. 2b, d in the supplementary material S4). Relative humidity larger than 98% was also detected during each foggy event at both altitudes of 1 m and 23 m. However, relative humidity measurements alone did not provide enough information to detect the onset and dissipation of fog, but we note that, in the case of the two longest events occurring on 24th November 2020 and 2nd February 2021, relative humidity was higher than 98% during the whole fog event at both altitudes. Figure 3 in the supplementary material S4 depicts data from four distinct longer (lasting more than 4 h) fog events, showcasing key

parameters observed by a ceilometer and PWD12 sensor. It encapsulates humidity, visibility, rain, and the SCI index values during these four foggy events. It can be seen from the Fig. 3 in the supplementary material S4 that fog duration indicated from visibility measurements was slightly smaller than fog duration shown by the ceilometer. Relative humidity remained higher than 95% at all levels during four fog events. Another common feature among these four fog events was the occurrence of mist before and after fog as per visibility measurements, indicating the possibility of mist getting transformed into fog under saturated conditions. Ceilometer reporting precipitation before and after fog are actually fog droplets settling down on the screen of ceilometer. This concise representation facilitates a comprehensive understanding of how these meteorological factors evolve during and around fog occurrences over time.

Almost all foggy events started in late evening or early morning and dissipated after sunrise due to the increase of shortwave radiation and the associated warming. The only exception was the longest fog event which formed on early morning November 24 and dissipated during the night of this day. Considering all the foggy events, the average relative humidity at altitude of 1 m was 99.96%, with a minimum value of 98% and maximum value of 100%. As clarified in the supplementary material S1,

Rh measurements are of limited accuracy whenever $Rh > 95\%$. The average wind speed was 0.97 m s^{-1} indicating calm conditions during fog. The average visibility was 423 m. The minimum value of 144 m was detected during the foggy event that occurred on 6th November 2020. The mean atmospheric longwave and surface outgoing longwave radiation were 323 W m^{-2} and 330 W m^{-2} , respectively. The mean net surface longwave radiation of -7 W m^{-2} indicates surface cooling.

3.2. Comparison of Friction Velocities and Sensible Heat Fluxes Observed at 2.5 m and 30 m

The fluxes were calculated using the TK3 software (Mauder & Foken, 2015). The input data for the TK3 software were the raw dataset, which with 10 Hz frequency obtained from there were recorded by sonic anemometer with frequency of 10 Hz was provided to the TK3 software. The following corrections available in TK3 were used for calculating the fluxes:

- Spike detection: Any values which exceed 4.5 times the standard deviation in a window of 15 values are labelled as spikes. For subsequent analysis values detected as spikes can be excluded for later calculation or can be substituted linearly by a value evaluated by linear interpolation.
- 2D coordinate rotation: Since our measurements are done on a flat terrain, we use 2D correction instead of planer fit method to make set the mean vertical wind component to zero.
- Correction of density fluctuations (Webb-Pearman-Leuning (WPL)-correction).
- Correction of spectral losses (Moore correction): It is applied to correct for the errors in of fluxes due to delayed frequency response.
- Schotanus correction: It corrects the fluctuation of sonic temperature into actual temperature fluctuations caused due to humidity effect. In our measurements, fast response measurements of water vapour were available to apply Schotanus correction in low level (CSAT-3 + EC150 in 2.5 m heights) and Bowen ratio for the Gill Solent Windmaster measurements in the 30 m level.

The covariances are maximized in TK3 by using cross correlation and by labelling the missing values in the data were treated with symbol of NaNs. The quality of the measured fluxes was determined by using the flag system described in Spoleto agreement, 2004 for CarboEurope -IP (Mauder & Foken, 2015). It has three classes, namely: Class 0: means high quality fluxes, Class 1: means moderate quality fluxes and Class 2: means low quality fluxes. The missing values in the data were treated as NaNs.

The friction velocities and sensible heat fluxes measured at 2.5 m and 30 m above the ground level (AGL) are compared (Fig. 3). The plot in Fig. 3a reveals that the friction velocity at height of 30 m was about 1.5 times larger than that one at height of 2.5 m. This indicates that the near-surface turbulent regime was not well developed, and this difference is the consequence of different flux footprints with surface inhomogeneity (see Fig. 4). In this case the theory about the constant flux layer for momentum fluxes cannot be applied. The varying surface roughness impacts the momentum exchange more significantly than the sensible or latent heat exchange. As a result, the values of sensible heat flux at the two levels were similar (Fig. 3b). The difference between the fluxes measured at the two different altitudes was only about 9%. This result is consistent with the assumption that the atmospheric surface layer can be considered as a constant flux layer for sensible heat exchange because the deviations below the 30 m layer was less than 10% under steady state and horizontally homogenous turbulence conditions (Panofsky & Dutton, 1984).

3.3. Calculation of Flux Footprint at 2.5 m and 30 m

Explanation of the different momentum fluxes measured at 2.5 m and 30 m levels can be found in the different footprint area. Flux footprint models use flux footprint function which is a probability density function for describing the contribution of each element of the upwind surface area to turbulence flux measurements from flux towers (Haszpra et al., 2022; Kljun et al., 2015). They are also used to estimate the position and sizes of surface source areas as well as contribution of passive scalars to the measured fluxes. The footprint area depends on the

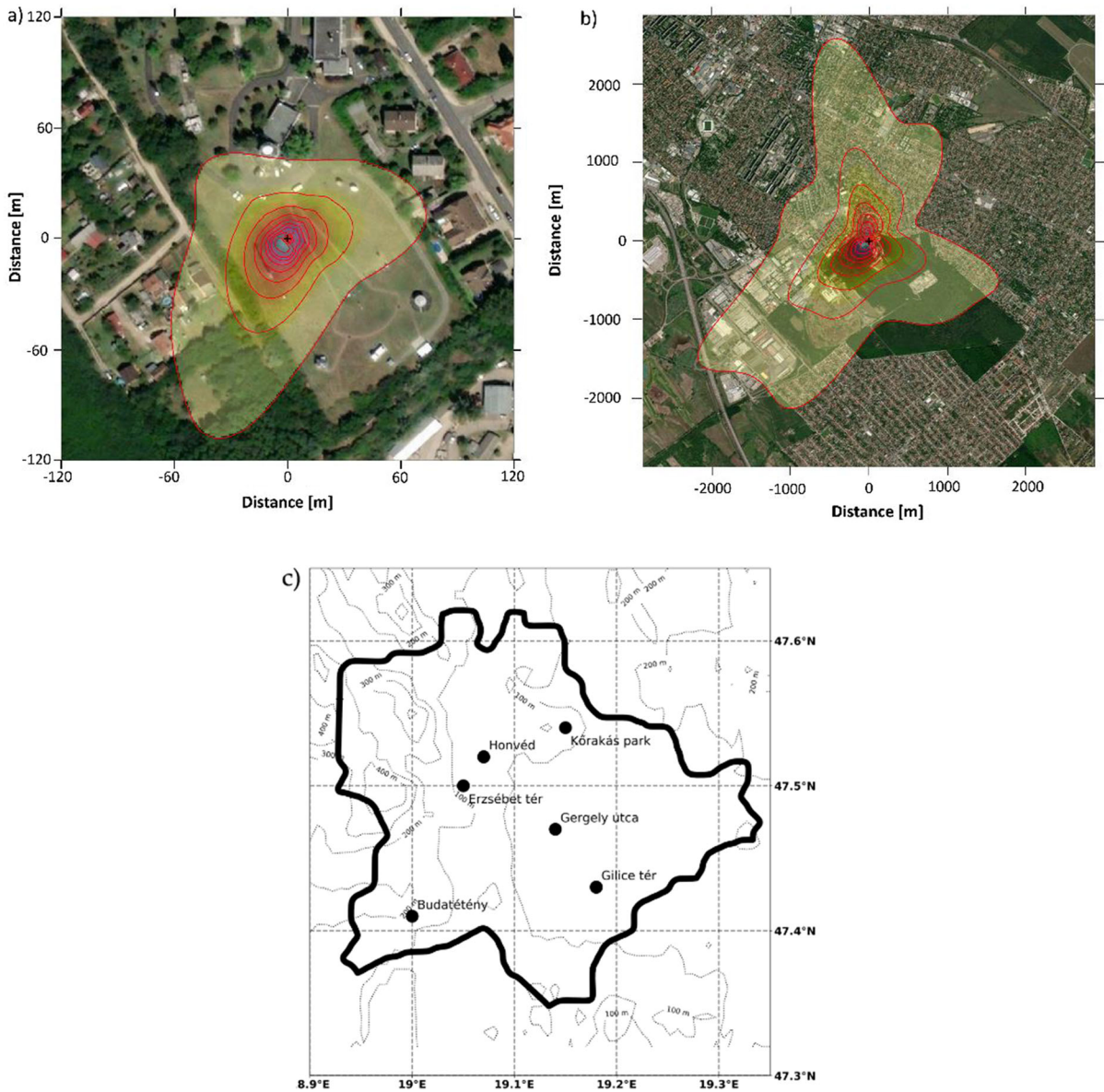


Figure 4

Flux footprints calculated at **a** 2.5 m (micrometeorological pole) and **b** 30 m tower (23rd November 12:00 UTC to 25th November 12:00 UTC). The micrometeorological pole and tower location is shown by a ' + ' symbol in both figures. The footprint contour lines (red) show a 10–90% contribution to the flux measurements in 10% steps **c**) the locations of main air pollution monitoring sites in Budapest, Pestszentlőrinc observatory (Fig. 1) is in the Gilice square (tér) after Varga-Balogh et al. (2020)

height of the eddy covariance system and the actual atmospheric conditions. The source areas are smaller in case of unstable stratification and larger in case of stable stratification. A flux measurement at a certain height is influenced by an area which can be 100 times the height of the measurement tower.

For calculation of the flux footprints, we have used the two-dimensional Flux Footprint Prediction model (FFP) of Kljun et al. (2015). This model is based on the LPDM-B backward Lagrangian stochastic particle dispersion model and provides an accessible parametrization for the LPDM-B model.

It also applies to a wide range of boundary layer stratifications and measurement heights. The model uses several parameters as input parameters for calculating flux footprints namely: measurement height above displacement height (z_m), roughness length (z_0), Obukhov length (L), standard deviation of lateral wind speed (σ_V), mean wind speed (V), and wind direction ($wind_dir$) at z_m , friction velocity (u_*) and height of the boundary layer (h). In our case, the Obukhov length, standard deviation of lateral wind speed, friction velocity and wind direction were either directly measured or calculated from the measurements. Either z_0 or V is required and if both are given z_0 is selected to calculate the footprint. FFP assumes stationarity and horizontal homogeneity of the flow over time periods of flux calculations (30 min in our case). The footprint at two heights ($z_m = 2.5\text{m}$ and 30 m) was calculated. We did not provide the data for z_0 , so mean wind speed (V), was used to calculate the footprint. Only the quality-controlled data was uploaded on the FFP online tool (Kljun et al., 2015). We did not provide the planetary boundary layer height (h) and it has been calculated for neutral and stable conditions according to the Appendix B of Kljun et al. (2015).

Figure 4a, b shows the footprint contributions of the surrounding area of the measurements to the flux measurements. Flux measurements at height of 2.5 m are mostly influenced by the open flat, grassy area with a few isolated obstacles (HungaroMet office buildings). This area impacted about 67% of the total number of the flux measurements. The comparison of values of u_* detected at 2.5 m and 30 m (Fig. 3a) show that the near surface turbulence was not well developed, because the observation point near the surface is obstructed by the nearby urban area and the forest.

Figure 4b shows that the flux footprint climatology characterizing the 30 m tower is affected by the nearby industrial area and by the urban forest which is located southwest of the tower. In this case almost 45% of data are determined by the nearby forest and industrial area. Since the mean roughness length of grassy-shrub area ($\sim 0.1\text{ m}$) is significantly smaller than that of a suburb or a forest ($\sim 1\text{ m}$) area, a flux divergence due to surface inhomogeneity was detected (Fig. 3a).

3.4. Case study. Radiation Fog Event on November 24, 2020

3.4.1 Synoptic Conditions

This section presents the analysis of the synoptic conditions along with the temporal evolution of the characteristics of the fog that occurred on 24th November (03:30–22:30 UTC), 2020 (duration was identified by ceilometer observation). The large-scale synoptic situation was as follows: An anticyclonic developed over Central and Southern Europe (Fig. 5a). The weather was initially determined by a wavy cold front along the edge of the cyclonic system north of the Carpathian Basin. The anticyclonic situation strengthened in the Carpathian Basin, leading to heavily cloudy and overcast situations prevailing during the morning hours of November 24 (Fig. 5b). The fog formed due to the development of a cold air pool with low wind speed in the Carpathian Basin. The HungaroMet daily weather reports reported that the air had cooled down to $-5\text{ }^\circ\text{C}$ during the early morning hours of 24th November resulting in formation of fog and stratus cloud in several regions of Hungary (https://met.hu/idojaras/aktualis_idojaras/napijelentes/). Thus, fog and low-level stratified clouds formed in the interior parts of Central and Eastern Europe and persisted due to the low temperature, high humidity, and low wind speeds. During the day, surface temperatures were between $0\text{ }^\circ\text{C}$ and $10\text{ }^\circ\text{C}$ in Hungary, and drizzle was observed in the later part of the day on 24th November. This drizzle is reported by the daily weather report of the HungaroMet for some areas surrounding Budapest. Here we are describing the large-scale synoptic situation and not the situation at the station. The amount of precipitation was not mentioned in the report. The weather of the next few days was also characterized by this anticyclonic weather situation.

3.4.2 Micrometeorological Conditions

Figure 6a–f summarizes the time evolution of the observed micrometeorological data for the foggy event that occurred on 24th November.

At the onset of fog, the relative humidity increases sharply at all levels. During the fog, relative humidity

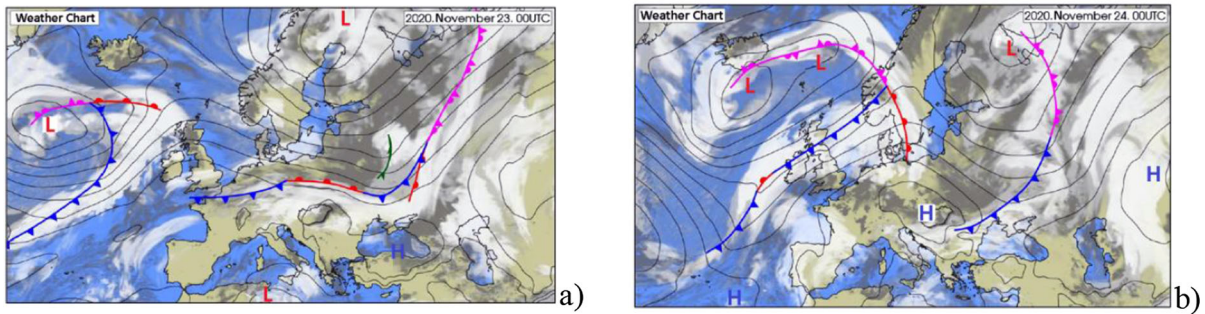


Figure 5

Synoptic conditions and frontal zones over Europe **a** on 23rd November at 00:00 UTC (left panel) and **b** on 24th November 24 at 00:00 UTC (right panel). Letters L (Low) and H (Height) denote the center of cyclones and that of anticyclone, respectively. Warm fronts, cold fronts and occluded fronts are denoted by red curved lines with semi circles, by blue curved lines with triangles, and by pink curved lines with semi circles and triangles, respectively. The green curved line assigns the location of the convergence line. White and gray color patches indicate the low and high cloud tops, respectively. The plots were obtained from the daily HungaroMet weather reports (https://met.hu/idojaras/aktualis_idojaras/napijelentes)

remained higher than 95% at all 4 levels. At the altitude of 1 m, it immediately increased to 100% after the onset of fog and remained at 100% throughout the foggy period. Relative humidity at other levels also reached the value of 100% (Fig. 6a), but only after the middle of the foggy event. The high relative humidity near the surface is also demonstrated by the leaf wetness data. The sudden increase of leaf wetness to one at 22:00 UTC on 23rd November indicates that the ground was wet due to the dew formation. The decrease of the leaf wetness at midday reveals that the surface became dry due to small increase of temperature (Fig. 6b). There was also a small decline in humidity values during the day on 24th November. This decline was very small as relative humidity decreased around 98% at 5 m and 9 m for a brief period.

Unfortunately, the ceilometer did not provide data including the cloud base height (CBH) between 4:30 and 9:30 UTC. CBH data and other parameters are detected from 9:30 UTC. (Our explanation is based on observation data and not on microphysical modelling.) The leaf wetness sensor shows dry conditions in this time, and we observe increase of temperature after 10:00 UTC at all of the 4 levels (for e.g., temperature at 1 m jumps from $-1\text{ }^{\circ}\text{C}$ to $0\text{ }^{\circ}\text{C}$ after 10:00 UTC). During this time, a slight negative long wave radiation budget was detected which coincides with temperature increase at all of the 4 levels.

Furthermore, the wind direction varied during this time period. All of these finding may be the consequence of the increase of the turbulent mixing resulting in the decrease of density of fog close to the surface.

The anticyclonic weather situation with the cold air pool helped the humidity values to remain higher for a few hours even after the fog dissipation. Consequently, relative humidity remained near saturation even after the dissipation of fog, which started at 22:30 UTC due to the forming of a low-level stratus cloud due to lifting up of the fog (see the time evolution of cloud base height in Fig. 6c). (It is a typical nighttime situation.)

The temperature decreased rapidly in the time period of 2–3 h before the onset of fog at all of the four levels. It dropped from $3\text{ }^{\circ}\text{C}$ to under $0\text{ }^{\circ}\text{C}$ between 23:00 UTC and 03:30 UTC. The temperatures at all the four levels were nearly the same and they remained below $1\text{ }^{\circ}\text{C}$ throughout the foggy period. We assume that the constant vertical profile of the temperature stems from the fact that radiative cooling at the top of the fog layer results in thermal homogenization and promotes the increase the depth of fog as suggested by Haeffelin et al. (2010).

Fog onset also goes together with the increase in LW budget from -50 W m^{-2} to 0 W m^{-2} resulting in surface cooling. After the fog onset the surface energy budget tends towards zero, so we detect nearly

constant temperature in the surface layer. The footprint of the *LW* instruments measuring the incoming and outgoing longwave radiation coincide and have same temperature and show the limiting/terminating radiative cooling of the surface. Fog dissipation was accompanied with a gradual increase in the temperature at all four levels which remained higher than 1 °C after 12:00 UTC on 25th November (Fig. 6b). This was attributed to the mixing, or/and local advection.

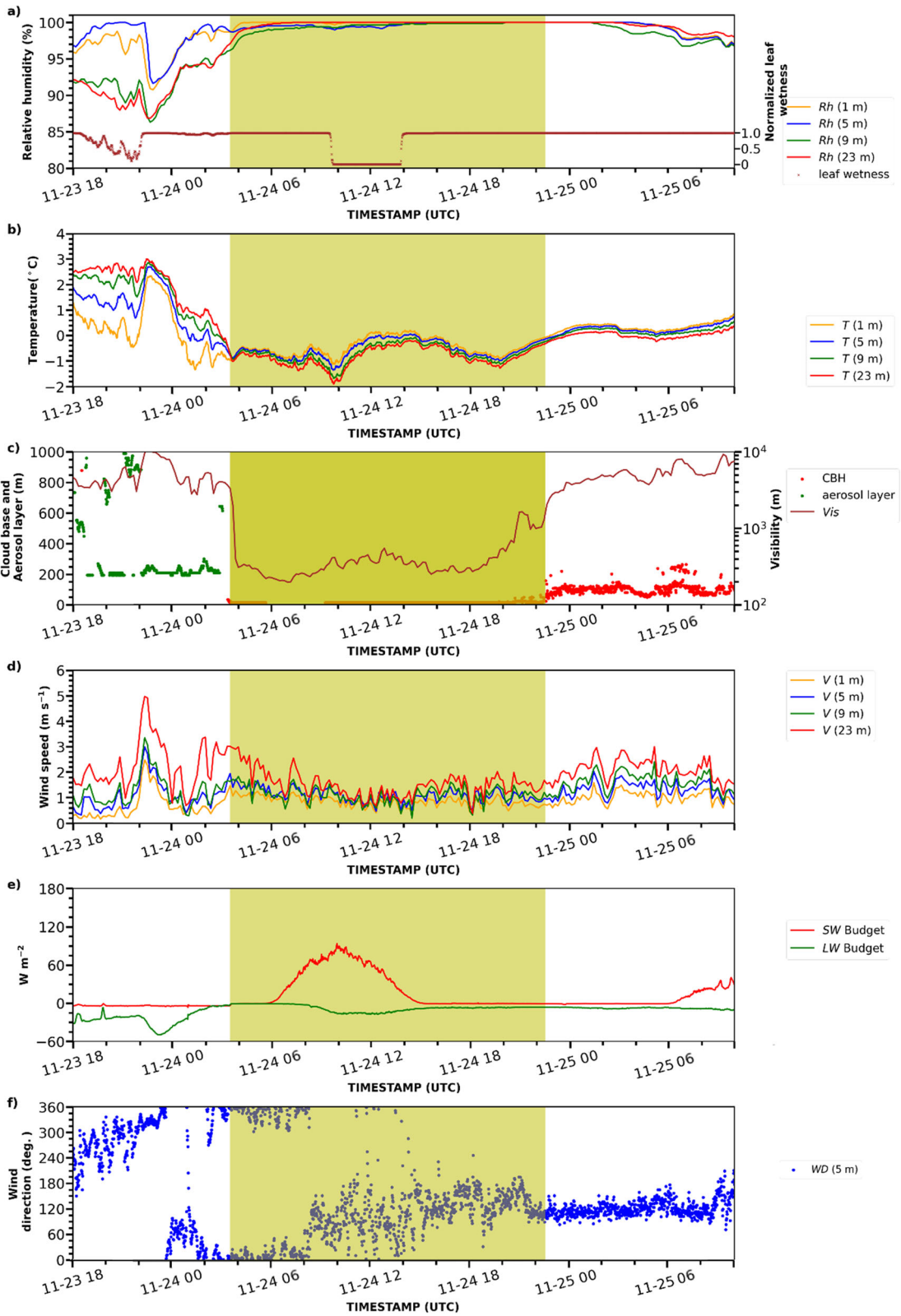
The net shortwave radiation budget (*SW*) remained lower than 100 W m^{-2} throughout the foggy period and decreased to less than 50 W m^{-2} on the next day due to the overcast sky conditions. The longwave radiation budget (*LW*) was close to 0 W m^{-2} during the whole foggy period and on the day after the fog as well. The fog and the low-level stratus clouds significantly mitigated the outgoing longwave radiation.

The time series of ceilometer backscatter profiles is plotted in Fig. 7. The ceilometers can measure cloud-base height of low-level clouds; however, they are rather inaccurate to give data about fog top height or vertical extension of the cloud (see the white area zone above the fog) due to the attenuation of the beam in the cloud (Nowak et al., 2008). Before the formation of fog, clear sky conditions were detected. The time of the sharp increase of backscatter signal (Fig. 7) agrees well with that of the steep decrease of the visibility (Fig. 6c). After 22:30 UTC on 24th November, the fog lifted gradually from the surface to a height above 100 m (see the red dots in Fig. 6c). The observed visibility remains less than 600 m until the time when the fog starts to lift from the surface. After the fog dissipation the cloud base remained at a height of around 200 m (Figs. 6c, and 7). A small amount of drizzle observed in the time period of 01:00–01:30 UTC on 25th November was produced by this low-level layer cloud. In this case the sedimentation of the drizzle might lead to transforming the fog into the elevated stratus cloud (Haeffelin et al., 2010). Figure 6a reveals that after the dissipation of the fog the decrease of relative humidity was the smallest at the highest altitude (23 m) where relative humidity was detected to be higher than all other levels. The reason for the gradual increase of relative humidity with height between surface and

cloud base could be the evaporation of drizzle which occurred between 01:00–01:30 UTC on 25th November. Another reason is that we assume that this may be attributed to sensor precision besides quality control (S1).

Figure 8 denotes time evolution of Turbulent Kinetic Energy (for unit mass) ($TKE = 1/2 (\sigma_u^2 + \sigma_v^2 + \sigma_w^2)$, where $\sigma_u, \sigma_v, \sigma_w$ are the standard deviations for each wind component) and that of momentum flux (τ). 5 to 6 h before the onset of fog, on the evening of 23rd November, a highly turbulent atmosphere was detected at altitudes of 2.5 m and 30 m. Maximum values larger than $0.6 \text{ m}^2 \text{ s}^{-2}$ and $0.1 \text{ kg m}^{-1} \text{ s}^{-2}$ was measured for TKE and momentum flux at 23:00 UTC on 24th November, respectively. The increase of wind speed at all the four levels (Fig. 6d) indicates the enhanced turbulent mixing. It is well known that mechanical turbulence enhanced by the wind leads to mixing of air masses and breaking of stable stratification (Cotton & Anthes, 2010). The plots in Fig. 6d suggest that the maximum value of the wind shear was $0.14 \text{ (m s}^{-1}) \text{ m}^{-1}$ as well as a change in wind direction at altitude of 5 m in time was also significant (Fig. 6f). The increase of turbulent kinetic energy and momentum flux must have resulted in vertical mixing causing the cooler air near the surface to mix with the warmer air layer above. This vertical mixing led to an increase of temperature at lower levels resulting in thermal homogenization (Fig. 6a). Later, due to the weakening of turbulence rapid cooling was generated by the negative longwave energy budget (Fig. 6e). The net radiation (which was equal with longwave net radiation) as shown in Fig. 10 was also negative and decreased, suggesting that as the air started to cool down it approached its dew point temperature and became saturated with moisture.

In this case study, except for a short time-period before the onset of the fog, the wind speed was below 2 ms^{-1} , and it slightly increases after the lifting of the fog (Fig. 6d). The fog has developed upwards from the surface up to 30 m within 30 min. The dependence of the time evolution of the relative humidity on the altitudes (Fig. 6a) suggests the radiative cooling resulted in the upward development of fog. During the foggy period the *TKE* and momentum flux were smaller than $0.4 \text{ m}^2 \text{ s}^{-2}$ and $0.06 \text{ kg m}^{-1} \text{ s}^{-2}$,



◀Figure 6

Time series of observed data before, during and after the foggy event which lasted from 03:30 UTC to 22:30 UTC on 24th November 2020). **a** relative humidity (Rh) at 4 levels, and normalized leaf wetness (0—dry, 1—wet, the data is displayed like Klemm et al. (2002), where high relative humidity coincides with high leaf wetness). **b** temperature (T) at 4 levels. **c** aerosol and fog layer/cloud base height observed by ceilometer, and visibility (Vis) observed by PWD12 sensor. **d** wind speeds (V) at 4 levels. **e** shortwave ($SW = G_s \downarrow + G_s \uparrow$), and longwave ($LW = G_l \downarrow + G_l \uparrow$), radiative balance. **f** wind direction at altitude of 5 m. The foggy period is denoted by shaded areas of yellow color. (The local time as CET is UTC + 1 h). The data cloud base height is not available between 5:00 to 9:30 UTC as there is no data available from the ceilometer during this period

respectively at both levels (Fig. 8). Li et al. (1999) and Nakanishi (2000) asserted that low values of turbulence could be measured before the fog formation and turbulence intensity can increase significantly as the fog transform from optically thin to optically thick fog. Other studies performed by Li et al. (2015) and Wang et al. (2021) have also found that during fog, TKE remained less than $1 \text{ m}^2 \text{ s}^{-2}$ and $0.4 \text{ m}^2 \text{ s}^{-2}$, respectively. The vertical wind speed variance (σ_w^2) decreased after the onset of fog (Fig. 8c). It remained less than $0.05 \text{ m}^2 \text{ s}^{-2}$ at altitude of 2.5 m during the fog event and increased after the dissipation of the fog.

Just before and after the fog event, the observed wind speed has a local minimum at all of the observation levels (Fig. 6d). TKE and σ_w^2 have similar trends, their values have a local minimum at one and

half hour before the onset of fog. At altitude of 2.5 m the TKE and σ_w^2 values decreased to less than $0.1 \text{ m}^2 \text{ s}^{-2}$ and $0.01 \text{ m}^2 \text{ s}^{-2}$, respectively. The radiative cooling resulted in stable stratification near the surface (see the time evolutions of the temperature observed at different altitudes (Fig. 6b). This stable layer weakened the turbulence before the fog formation.

Wind speeds increased once again on the early morning of 25th November after a short calm period following fog dissipation. Increase of the wind speeds, TKE and momentum flux was promoted by the gradual increase of the surface temperature. This process increased the depth of surface mixing layer and enhanced the entrainment at the top of the fog. This increase in the depth of surface mixing layer is clearly demonstrated by the lifting up the fog as the cloud base height gradually increased above 100 m after 22:00 UTC on November 24 (Figs. 6c and 7). Cloud base remained at a height above 100 m on 25th November evening after 20UTC (The local time is CET, which is UTC + 1 h).

3.4.3 Boundary Layer Profiles

Characteristics of the vertical profiles of virtual potential temperature (Θ_v), wind speed (V) and relative humidity (Rh) before, during and after the fog occurrence have been studied by analyzing radiosonde observations (Budapest, 12843). The depth of the fog was evaluated by examining the radiosonde profiles (Temimi et al., 2020) because the ceilometer

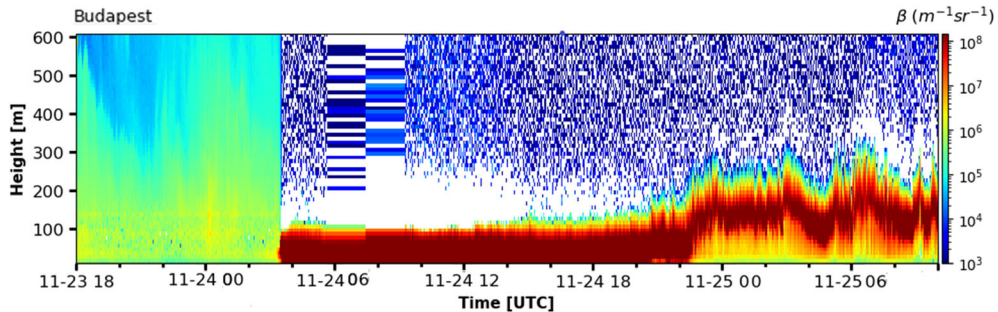


Figure 7

Time-series of ceilometer backscatter profile indicates the cloud base or low-level stratus cloud which transformed into fog on 24th November. The dark red zone with the highest values of backscatter signals shows the presence of fog. β here refers to the attenuated backscatter signal. (From 5:00 to 9:30 UTC the data from ceilometer is not available due to malfunctioning of data acquisition system.)

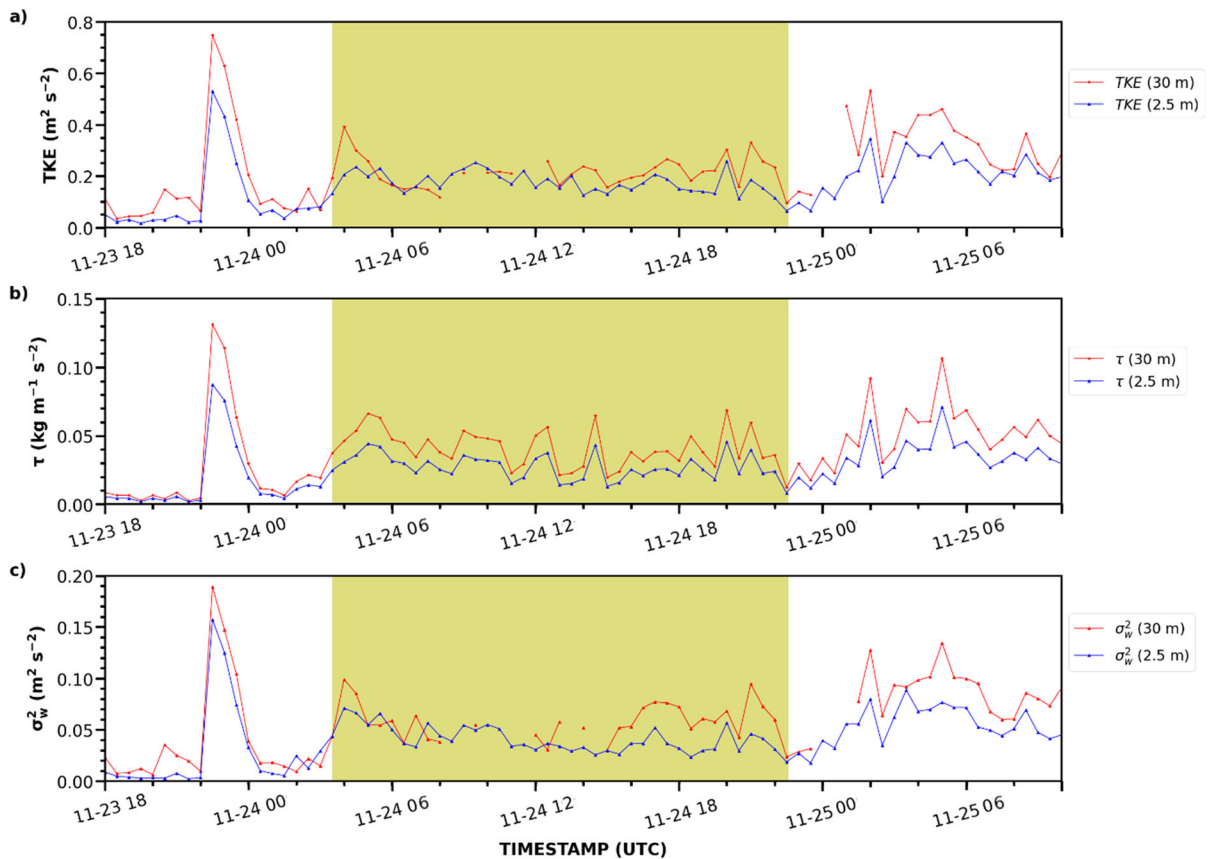


Figure 8

Time series of turbulent parameters before, during and after the foggy event **a** Turbulent kinetic energy (TKE) at altitudes of 2.5 m (blue) and 30 m (red), **b** Momentum flux (τ) at altitudes of 2.5 m (blue) and 30 m (red), **c** Vertical wind speed variance (σ_w^2) at altitudes of 2.5 m (blue) and 30 m (red). The foggy period is shaded with yellow color. Turbulent fluxes were evaluated by using TK3 software with an averaging time of 30 min

beam cannot penetrate dense fog. The optimal solution of estimation would be cloud radar (Bell et al., 2021) which was not available.

Before the fog occurrence (November 24, 00:00 UTC) the virtual potential temperature gradually increased with height up to ≈ 400 m indicating a stable atmospheric layer (Fig. 9a). As a result, vertical motions and mixing are inhibited due to stable atmospheric conditions that supported fog development during the late night, after 03:30 UTC. Temimi et al. (2020) analyzed observational data about 14 fog events, and they asserted that the strength and persistence of the near-surface temperature inversion significantly controlled the fog development. In two intensively analyzed cases they found that inversion formed 3–5 h before the onset of

fog and extended up to the depth of 800 m. Egli et al. (2015) also observed a strong ground touching inversion layer during the fog events in their study.

In the middle of the foggy period (24th November at 12:00 UTC), the virtual potential temperature close to the surface is smaller than that before fog onset and is near constant up to the height of about 220 m. This indicates neutral atmospheric stability (Fig. 9a). The jump of virtual potential temperature could be seen at the altitude of about 220 m during fog, the event indicating the presence of strong inversion. The top of inversion layer could be identified by a sudden increase of virtual potential temperature ($\Delta\Theta_v \approx 2.5^\circ\text{C}$). Above the height of 125 m, the virtual potential temperature increases slowly with height, indicating that a weak stable layer had formed

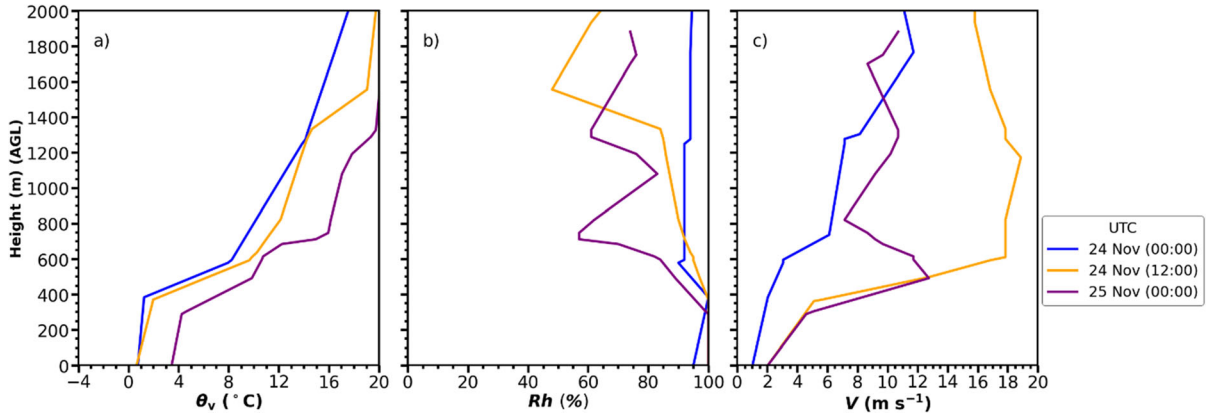


Figure 9

Vertical profiles of **a** virtual potential temperature (Θ_v), **b** relative humidity (Rh) and **c** wind speed (V). The profiles were derived from radiosonde data (Budapest, 12843). The time of the soundings is denoted by different colors (Budapest (12843), from November 24, 00:00 to November 25, 00:00 of 2020)

in the upper part of the inversion (125–220 m). The stable layer decoupled the fog layer from the layer of air above and this strong inversion might have prevented the upward spreading of the fog. Based on the ceilometer measurements the top of the fog was within the range of 100–125 m. But vertical extension of fog has been underestimated by the ceilometer with the range of about 53 ± 32 m in some studies (Nowak et al., 2008) because it has limitations in detecting fog or cloud tops. The white zone above the ‘fog’ in ceilometer backscatter profiles in Fig. 7 indicates this uncertainty.

Stable atmospheric conditions can be observed on 25th November, at 00:00 UTC as virtual potential temperature (Θ_v) increased with height. The inversion also increased, and a constant potential temperature gradient was observed. The altitude of the strong inversion layer (600 m) corresponds to the top of the low-level stratus formed due to the lifting up of the fog.

The vertical profile of the relative humidity (Rh) is in line with the vertical extent of the fog (12:00 UTC) and the fog top can be detected between 250 to 300 m (Fig. 9b). It can be concluded that during the fog, the surface layer (up to 220 m) was saturated, and wind was calm and remained around 1 m s^{-1} up to the height of 250 m, clearly indicating the top of fog (see sounding at 12:00 UTC on November 24 in Fig. 9c).

Temimi et al. (2020) also concluded that the high vapor content in the near surface layer and low wind speeds ($0.5\text{--}1 \text{ m s}^{-1}$) are necessary for radiation fog formation. The presence of low wind speed leads to weaker turbulence. Our results and observation concur with Boutle et al. (2018) who found that the saturated conditions close to the surface and above promoted the deepening of fog. They also reported that the fog initially formed under stable conditions with inversion, and weak turbulence was found before fog onset.

After the fog had dissipated (00:00 UTC on November 25), the wind speed increased significantly below the altitude of 600 m. By 00:00 UTC on 25th November the cloud top was detected at about 200 – 300 m height by the ceilometer.

3.4.4 The Surface Energy Budget

The time evolution of the components of the surface energy budget components is depicted in Fig. 10. The maximum values of net radiation (Rn) were smaller than 70 W m^{-2} during the fog. While the values of the sensible heat fluxes (H) were around 30 W m^{-2} , the latent heat fluxes (LE) was smaller than 10 W m^{-2} (Fig. 10). The maximum value of the net radiation was smaller than 25 W m^{-2} on the next cloudy day resulting in sensible and latent heat fluxes barely larger than zero. Unfortunately, the quality of

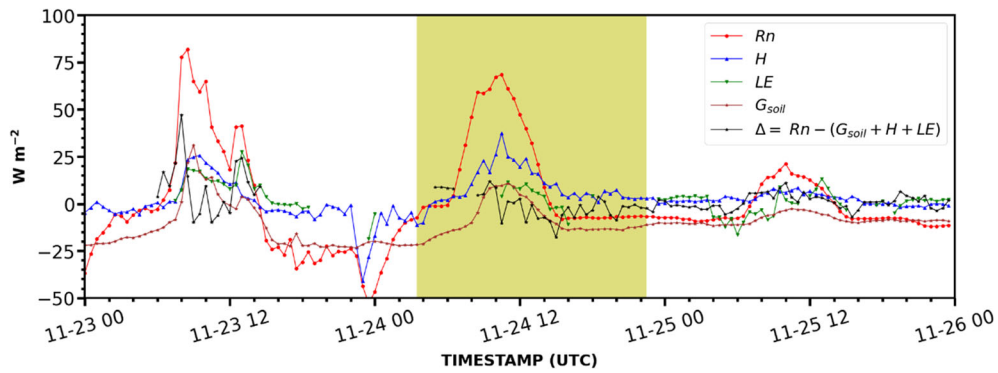


Figure 10

Time series of components of surface energy budget. Net radiation (R_n), sensible heat flux (H), latent heat flux (LE), the heat flux into the soil (G_{soil}) and the residual term ($\Delta = R_n - (G_{soil} + H + LE)$). The foggy period is shaded with yellow color.

the 30 min time averaged latent heat fluxes observed on 24th and 25th of November was low and a lot of latent heat flux data had to be filtered out (Fig. 10). Due to the small absolute fluxes, the half-hourly Bowen ratio values ($\beta = H/LE$) showed high variability when calculated using 30 min averaged fluxes. Figure 11 displays the calculated Bowen ratios before, during and after the fog, which varied between 1.10 ± 0.48 , 2.46 ± 0.54 and 1 ± 0.56 during daytime on 23rd, 24th, and 25th November, respectively. We can see that the Bowen ratio calculated using this method showed high uncertainty due to low quality latent heat fluxes.

The value of Bowen ratio was also calculated from the profile data of temperature and relative humidity using the gradient method in the 1–5 m

layer. The Bowen ratio varied between 1.09 ± 0.28 , 0.86 ± 0.13 and 0.79 ± 0.10 during the daytime period on 23rd, 24th (foggy day) and 25th of November respectively. The values of Bowen ratio on 23rd November calculated using both methods agree well even though the former shows higher uncertainty. For the foggy day of 24th November, a much higher differences are detected but both methods provide positive Bowen ratio values which indicate that some evaporation occurred from the surface between 10:00–14:00 UTC.

If we know the available energy and the gradient Bowen ratio, we assume that there is no closing error in the energy balance. This is not fulfilled in our case. The deviations of the Bowen ratio calculated in the two ways indicate the uncertainties in the

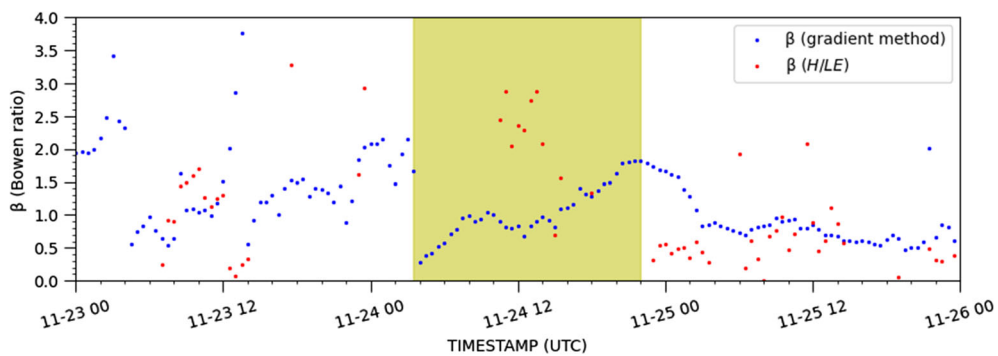


Figure 11

Bowen ratio (β) before, during and after the foggy event calculated using the 30-min averaged fluxes (red points) and gradient method in the 1–5 m layer (blue points)

measurements. We analyze the ratio of small absolute value turbulent currents and gradients. As mentioned before, many data points had to be filtered out because of the low quality of the eddy covariance latent heat fluxes. Thus, the continuously available gradient Bowen ratio is additional information.

During the foggy event (shaded with yellow color) slightly unstable (near-neutral) stratification was detected. The temperature at 23 m level was little bit lower than at 1 m level. The differences remained below 0.2 °C throughout the foggy event (Fig. 6b). In the daytime, when net radiation was above 70 W m⁻², we can detect dry surface (leaf wetness is 0, see Fig. 6a) which indicates a positive latent and sensible heat fluxes (Fig. 10).

The surface was wet as per the leaf wetness sensor, but the CS616 soil moisture sensor installed at 5 cm deep detected mean soil moisture content of 16 Vol.% during the whole foggy event as well as on the next day. (The maximum soil moisture value during the whole experiment was 27 Vol.%) Furthermore, the sensible, latent, and ground heat fluxes remained low due to very small net radiation. The heat flux into the soil (G_{soil}) has been calculated by using the temperature and soil moisture profiles observed in the upper 8 cm soil layer, and the self-calibrating heat flux sensors positioned at the bottom of this layer. The heat capacity for dry soil (840Jkg⁻¹K⁻¹) was used to evaluate the heat flux in the soil (Horváth et al., 2018; Liebenthal & Foken, 2007). The closure term of the energy budget (except at three 30-min data points) had a variation of ± 20 W m⁻² throughout the analyzed 3-day period, which is an acceptable range. The energy budget closure (EBC), $100 \bullet \sum_i [H_i + LE_i] / \sum_i [Rn_i - (G_{soil})_i]$ was around 81.2%.

A comprehensive energy budget closure (EBC) analysis performed by Wilson et al (2002) revealed that the average of EBC imbalance was about 20%. The imbalance was demonstrated in all types of vegetation and that of climates. Rahman et al (2019) showed that during winter the EBC was 0.65 due to the foggy and snowy weather conditions. Jin et al. (2022) asserted that during the foggy cool season, the energy budget closure with an EBC of 0.53 was rather typical. They also observed smaller energy fluxes and insufficient turbulence development

resulting in poor energy closure. Therefore, analysis of more sites could give a clear picture about the mean energy imbalance during foggy situations in Hungary.

3.4.5 Local Effects

In this section, standard meteorological and micrometeorological sensors were used to quantify local effects during this radiation type fog event. Two important local effects were found which influence the formation of fog in this case study.

- i) Development of nighttime stable surface layer before the formation of radiation fog: The wind speed on 23rd November in the time period of 16:00–22:30 UTC did not exceed 2.5 m s⁻¹ at altitude of 23 m and was below 1 m s⁻¹ at level 1 m above the surface (Fig. 6d). The temperature difference between the altitudes of 23 m and 1 m (the temperature increases by about 2.5 °C between these two levels) at 22:30 UTC (Fig. 6b) demonstrates well the formation of the stable layer. During the time period prior to the fog formation, the relative humidity increased from 93–94% and became closer to saturation (98–99%) at altitudes of 1 m and 5 m, however it remained around 90% at altitudes of 9 m and 23 m (Fig. 6a). On the other hand, the net radiation was small with about -25 W m⁻², and the available energy ($Rn - G$) was also about 25 W m⁻². The sensible heat flux (H) values were close to zero as well based on the measured energy budget components (Rn , G_{soil} , H) (Fig. 10). However, due to turbulent mixing during a short time period before fog formation (at about 23:00 UTC), the temperature increased at the lower levels due to mixing.
- ii) Effect of turbulent mixing (23rd November 22:30 UTC–24th November 00:00 UTC): The temporal increase of the wind shear near the surface due to wind speed increased up to 6 m s⁻¹ at the altitude of 23 m enhanced the TKE and momentum fluxes (Figs. 6d and 8). As a result of that a well-mixed surface layer was developed, and temperature difference between the altitudes of 1 and 23 m were smaller than 0.4 °C. Later, due to a negative longwave energy budget and larger deficit of net

radiation (-50 W m^{-2}) as well as higher negative sensible heat flux, we observed a decrease in temperature at 1 m and subsequently at all the four levels. Just before the onset of fog, a slight increase in *TKE* and momentum flux can be observed this led to thermal homogenization and promoted upward fog development.

4. Conclusions

The Budapest fog experiment was carried out during the winter period of 2020/2021 at the main observatory of the HungaroMet located in the suburban area of Budapest (Figs. 1 and 4). 23 fog events were detected. The onset of all the fog events happened in late evenings or night and they were categorized either as radiation or cloud base lowering fog. Except for one, all the foggy events dissipated in the morning. The observation data about longest radiation fog event (19 h) occurring in November 2020 during an anticyclonic synoptic situation are analysed in this study. The combination of slow and fast response sensors enabled us to evaluate the radiation and surface energy budget components at the measurement site. This experiment has provided us the following key understandings and lessons with regards to fog lifecycle:

- Uncertainty of the relative humidity measurements near the saturation: A semi-empirical recalculation method should be applied for correcting *Rh* data if the relative humidity is larger than 85%.
- Uncertainties in detection of fog duration: Compared to the ceilometer data, the Present Weather sensor provide shorter the duration of fog periods with an average value of 9%. This discrepancy is the consequence of the different measurement principle of both the instruments.
- The SCI index evaluated by the ceilometer suggested rain before and after foggy events more frequently because the sedimentation of fog drops was detected by the ceilometer as rain drops. The precipitation data provided by the ceilometer are not reliable in such cases.
- Flux divergences in sonic anemometer measurements: Correlations between the friction velocities

at the heights of 2.5 m and 30 m and similarly for the sensible heat fluxes evaluated from the observed data above a complex terrain revealed that the relationship between the data observed was linear both for the friction velocity (slope: 1.55, R^2 : 0.85) and sensible heat flux (slope: 0.91, R^2 : 0.85). The friction velocity at height of 30 m was 1.5 times higher than that at 2.5 m. This is the consequence of different flux footprints due to surface inhomogeneity above a suburban area with limited fetch. These are well-known effects, but it is also important to quantify these effects for different regions based on flux measurements and footprint calculations.

- Turbulence and fog occurrence: Fog formed from the surface upwards in the radiative fog case. Low to moderate turbulence can promote the upward development of fog under saturated conditions. Our observation suggests that during the fog the *TKE* and momentum fluxes remained smaller than $0.4 \text{ m}^2 \text{ s}^{-2}$ and $0.06 \text{ kg m}^{-1} \text{ s}^{-2}$ near the surface, at an altitude of 2.5 m. Other studies performed in Canada (Wang et al., 2021) and in China (Li et al., 2015) also found that *TKE* values remained smaller than $1 \text{ m}^2 \text{ s}^{-2}$ and $0.4 \text{ m}^2 \text{ s}^{-2}$ during fog, respectively. The ParisFog experiment also showed that fog started to develop when *TKE* values reached a local minimum at both 10 and 30 m heights, and a minimum of $0.2 \text{ m}^2 \text{ s}^{-2}$ was recorded. During the fog events *TKE* values remained below $1 \text{ m}^2 \text{ s}^{-2}$ in ParisFog experiment as well. The weakness of the vertical mixing is illustrated by the small value of σ_w^2 , whose value remained lower than $0.05 \text{ m}^2 \text{ s}^{-2}$ during the foggy period. Other studies (Fernando et al., 2021; Ghude et al., 2017; Price, 2019; Price et al., 2018) also asserted that a near saturated atmosphere close to the surface and moderate turbulence promoted the fog development, and the fog was likely persistent if $0.005 \text{ m}^2 \text{ s}^{-2} < \sigma_w^2 < 0.01 \text{ m}^2 \text{ s}^{-2}$. In our case, the observed σ_w^2 was higher.
- Radiosonde profiles: The presence of inversion and stable atmospheric conditions could be identified before fog onset. The virtual potential temperature close to the surface 2–3 h before fog onset is higher than that during the foggy period. Formation of inversion and high potential temperature near

the surface 2 to 3 h prior to fog onset has been identified by Ghude et al. (2017) and Shen et al. (2018). Ghude et al. (2017) demonstrates that it can serve as a good indicator for fog forecasting. Near the surface weakly unstable stratification or near neutral conditions persist during foggy weather. An inversion layer formed above near neutral layer due to the radiative cooling at the top of the fog.

- Special micrometeorological features during the case study: A well-developed stable surface layer disappeared due to the temporal, local increase of wind shear. As a result of stronger turbulent mixing, temperatures increased at all levels before the fog event. Later, small wind speed, stable nighttime stratification, and the neat radiation effect resulted in radiative cooling which resulted in fog formation. During the daytime we observed net radiation to be higher than 70 W m^{-2} with positive sensible and latent heat fluxes even though fog persisted. A temporal, slight change in leaf wetness (from wet to dry) indicated that evaporation happened for a short period from the surface. Further low turbulence intensities also allowed the fog to persist.

Study of surface layer profiles of different meteorological variables and energy budget components can improve our understanding about surface micrometeorological processes that occur in fog. In the next phase of this research a comprehensive study is planned by involving more observed cases and using numerical model simulation as well. Specifically, it can lead to development and testing of new surface layer parametrization as well as the impact of cooling rate on the formation of fog (Cuxart et al., 2021; Kumar & Schmeller, 2022; Peterka et al., 2024).

Acknowledgements

The authors would like to thank the Hungarian Meteorological Service (HungaroMet, Budapest, Hungary) for providing the required meteorological datasets. The authors would also like to thank Peter K. Musyimi for professional language check and proofreading the manuscript.

Author Contributions Conceptualization: A.G., A.V.T, I.G. and T.W.; Methodology: A.G., I.G. and T.W.; Formal analysis: A.G., A.P., A.V.T, I.G. and T.W.; Measurements and data base: all authors; Data curation: A.G., A.V.T, P.T., A.R., Gy.H., Z.F., and T.W.; Writing—original draft preparation: A.G., I.G., P.T. and T.W.; Writing—review and editing: A.G., A.V.T, I.G., P.T. and T.W.; Visualization: A.G.; Supervision: I.G., K.I. and T.W.; Funding acquisition: I.G., P.T. and T.W. All authors have read and agreed to the published version of the manuscript.

Funding

Open access funding provided by Eötvös Loránd University. The measurement campaign was performed in the frame of GINOP2.3.2-15-2016-00007, GINOP-2.3.2-15-2016-00055, OTKA-138176 and CA20108-FAIR NETwork of micrometeorological measurements (FAIRNESS) COST Action. The experiment is connected with the PANNEX program which is part of the Regional Hydroclimate Project (RHP) of the World Climate Research Programme (WCRP).

Data Availability

The eddy-covariance and meteorological observations are available from the authors upon request.

Declarations

Conflict of interest The authors have no conflict of interest.

Institutional review board statement Not Applicable.

Informed consent statement Not Applicable.

Open Access This article is licensed under a Creative Commons Attribution 4.0 International License, which permits use, sharing, adaptation, distribution and reproduction in any medium or format, as long as you give appropriate credit to the original author(s) and the source, provide a link to the Creative Commons licence, and indicate if changes were made. The images or other third party material in this article are included in the article's Creative Commons licence, unless indicated otherwise in a credit line to the material. If material is not included in the article's Creative Commons licence and your intended use is not permitted by statutory regulation or exceeds the permitted use, you will need to obtain permission directly from the copyright holder. To view a copy of this licence, visit <http://creativecommons.org/licenses/by/4.0/>.

Publisher's Note Springer Nature remains neutral with regard to jurisdictional claims in published maps and institutional affiliations.

REFERENCES

- Baklanov, A., Brunner, D., Carmichael, G., Flemming, J., Freitas, S., Gauss, M., Hov, Ø., Mathur, R., Schlünzen, K. H., Seigneur, C., & Vogel, B. (2017). Key issues for seamless integrated chemistry-meteorology modeling. *Bulletin of American Meteorological Society*, 98(11), 2285–2292. <https://doi.org/10.1175/BAMS-D-15-00166.1>
- Bari, D. (2019). A preliminary impact study of wind on assimilation and forecast systems into the one-dimensional fog forecasting model COBEL-ISBA over Morocco. *Atmosphere*, 10(10), 615. <https://doi.org/10.3390/atmos10100615>
- Bell, A., Martinet, P., Caumont, O., Vié, B., Delanoë, J., Dupont, J.-C., & Borderies, M. (2021). W-band radar observations for fog forecast improvement: An analysis of model and forward operator errors. *Atmospheric Measurement Techniques*, 14, 4929–4946. <https://doi.org/10.5194/amt-14-4929-2021>
- Bergot, T., Terradellas, E., Cuxart, J., Mira, A., Liechti, O., Mueller, M., & Nielsen, N. W. (2007). Radiation fog, numerical weather prediction. *Journal of Applied Meteorology and Climatology*, 46(4), 504–521. <https://doi.org/10.1175/JAM2475.1>
- Bodaballa, J. K., Geresdi, I., Ghude, S. D., & Salma, I. (2022). Numerical simulation of the microphysics and liquid chemical processes occur in fog using size resolving bin scheme. *Atmospheric Research*, 266, 105972. <https://doi.org/10.1016/j.atmosres.2021.105972>
- Boutle, I., Price, J., Kudzotsa, I., Kakkola, H., & Romakkaniemi, S. (2018). Aerosol–fog interaction and the transition to well-mixed radiation fog. *Atmospheric Chemistry and Physics*, 18(11), 7827–7840. <https://doi.org/10.5194/acp-18-7827-2018>
- CHM 15k Manual by Luft (2019). *Manual cloud height sensor CHM 15k*. Luft Mess und Regeltechnik https://s.campbellsci.com/documents/ca/manuals/chm15k_man.pdf
- Cotton, W.R., & Anthes, R.A. (2010). *Storm and cloud dynamics*. Academic Press, Second edition, 809 p. ISBN: 9780080916651
- Cséplő, A., Sarkadi, N., Horváth, Á., Schmeller, G., & Lemler, T. (2019). Fog climatology in Hungary. *Időjárás*, 123(2), 241–264. <https://doi.org/10.28974/idojaras.2019.2.7>
- Cuxart, J., Telisman Prtenjak, M., & Matjacic, B. (2021). Pannonian basin nocturnal boundary layer and fog formation: Role of topography. *Atmosphere*, 12, 712. <https://doi.org/10.3390/atmos12060712>
- Description of Sounding Columns, University of Wyoming [Online] (2022, June 20). <http://weather.uwyo.edu/upperair/sounding.html>
- Dhangar, N. G., Lal, D. M., Ghude, S. D., Kulkarni, R., Parde, A. N., Pithani, P., Niranjan, K., Pprasad, D. S. V. V. D., Jena, C., Sajjan, V. S., Prabhakaran, T., Karipot, A. K., Jenamani, R. K., Singh, S., & Rajeevan, M. (2021). On the conditions for onset and development of fog over New Delhi: An observational study from the WiFEX. *Pure and Applied Geophysics*, 178(9), 3727–3746. <https://doi.org/10.1007/s00024-021-02800-4>
- Dorman, C. E., Hoch, S. W., Gultepe, I., Wang, C. Q., Yamaguchi, R. T., Fernando, H. J. S., & Krishnamurthy, R. (2021). Large-scale synoptic systems and fog during the C-FOG field experiment. *Boundary-Layer Meteorology*, 181, 171–202. <https://doi.org/10.1007/s10546-021-00641-1>
- Duynkerke, P. G. (1999). Turbulence, radiation and fog in Dutch stable boundary layers. *Boundary-Layer Meteorology*, 90(3), 447–477. <https://doi.org/10.1023/A:1026441904734>
- Egli, S., Maier, F., Bendix, J., & Thies, B. (2015). Vertical distribution of microphysical properties in radiation fogs—A case study. *Atmospheric Research*, 151, 130–145. <https://doi.org/10.1016/j.atmosres.2014.05.027>
- Feigenwinter, C., Franceschi, J., Larsen, J. A., Spirig, R., & Vogt, R. (2020). On the performance of microlysimeters to measure non-rainfall water input in a hyper-arid environment with focus on fog contribution. *Journal of Arid Environments*, 182, 104260. <https://doi.org/10.1016/j.jaridenv.2020.104260>
- Fernando, H. J., Gultepe, I., Dorman, C., Pardyjak, E., Wang, Q., Hoch, S. W., Richter, D., Creegan, E., Gaberšek, S., Bullock, T., & Hocut, C. (2021). C-FOG: Life of coastal fog. *Bulletin of American Meteorological Society*, 102(2), 244–272. <https://doi.org/10.1175/BAMS-D-19-0070.1>
- Gandhi, A., Bartok, B., Ilona, J., Musyimi, P. K., & Wedinger, T. (2022). Historical fog climate dataset for Carpathian Basin from 1886 to 1919. *Data in Brief*, 44, 108500. <https://doi.org/10.1016/j.dib.2022.108500>
- Ghude, S.D., Bhat, G.S., Prabhakaran, T., Jenamani, R.K., Chate, D.M., Safai, P.D., Karipot, A.K., Konwar, M., Pithani, P., Sinha, V., Rao, P.S.P., Dixit, S.A., Tiwari, S., Todekar, K., Varpe, S., Srivastava, A.K., Bisht, D.S., Murugavel, P., Ali, K., Mina, U., Dhruva, M., Rao, Z.J., Padmakumari, B., Hazra, A., Nigam, N., Shende, U., Lal, D.M., Chandra, B.P., Mishra, A.K., Kumar, A., Hakkim, H., Pawar, H., Acharja, P., Kulkarni, R., Subharthi, C., Balaji, B., Varghese, M., Bera, S., & Rajeevan, N. (2017). Winter fog experiment over the Indo-Gangetic plains of India. Winter fog experiment over the Indo-Gangetic plains of India. *Current Science*, 112(4), 767–784. <http://www.jstor.org/stable/24912578>, <https://doi.org/10.18520/CS/V112/I04/767-784>
- Griesel, S., Theel, M., Niemand, H., & Lanzinger, E. (2012). Acceptance test procedure for capacitive humidity sensors in saturated conditions. *WMO CIMO TECO-2012*, Brussels, Belgium, pp. 1–7. <https://api.semanticscholar.org/CorpusID:114702066>
- Gulpepe, I. (ed.). (2008). *Fog and boundary layer clouds: fog visibility and forecasting*. Birkhäuser Verlag AG, Basel, Boston, Berlin, 262 p. ISBN 978-3-7643-8418-0
- Gulpepe, I., Fernando, H. J. S., Pardyjak, E. R., Hoch, S. W., Silver, Z., Creegan, E., Leo, L. S., Pu, Z., De Wekker, S. F. J., & Hang, C. (2016). An overview of the MATERHORN fog project: Observations and predictability. *Pure and Applied Geophysics*, 173(9), 2983–3010. <https://doi.org/10.1007/s00024-016-1374-0>
- Gulpepe, I., Kuhn, T., Pavolonis, M., Calvert, C., Gurka, J., Heymsfield, A. J., Liu, P. S. K., Zhou, B., Ware, R., Ferrier, B., & Milbrandt, J. (2014). Ice fog in arctic during FRAM-Ice fog project: Aviation and nowcasting applications. *Bulletin of American Meteorological Society*, 95(2), 211–226.
- Gulpepe, I., Tardif, R., Michaelides, S. C., Cermak, J., Bott, A., Bendix, J., Müller, M. D., Pagowski, M., Hansen, B., Ellrod, G., & Jacobs, W. (2007). Fog research: A review of past achievements and future perspectives. *Pure and Applied Geophysics*, 164(6), 1121–1159. <https://doi.org/10.1007/s00024-007-0211-x>

- Haeffelin, M., Bergot, T., Elias, T., Tardif, R., Carrer, D., Chazette, P., Colomb, M., Drobinski, P., Dupont, E., Dupont, J. C., & Gomes, L. (2010). ParisFog: Shedding new light on fog physical processes. *Bulletin of American Meteorological Society*, 91(6), 767–783. <https://doi.org/10.1175/2009BAMS2671.1>
- Hang, C., Nadeau, D. F., Gulpepe, I., Hoch, S. W., Román-Cascón, C., Pryor, K., Fernando, H. J. S., Creegan, E. D., Leo, L. S., Silver, Z., & Pardyjak, E. R. (2016). A case study of the mechanisms modulating the evolution of valley fog. *Pure and Applied Geophysics*, 173(9), 3011–3030. <https://doi.org/10.1007/s00024-016-1370-4>
- Haszpra, L., Barcza, Z., Ferenczi, Z., Hollós, R., Kern, A., & Kljun, N. (2022). Real-world wintertime CO, N₂O, and CO₂ emissions of a central European village. *Atmospheric Measurement Techniques*, 15(17), 5019–5031. <https://doi.org/10.5194/amt-15-5019-2022>
- Horváth, L., Koncz, P., Möring, A., Nagy, Z., Pintér, K., & Weidinger, T. (2018). An attempt to partition stomatal and non-stomatal ozone deposition parts on a short grassland. *Boundary-Layer Meteorology*, 167(4643), 303–326. <https://doi.org/10.1007/s10546-017-0310-x>
- Houze, R. A., & Houze, R. (2019). Cloud and weather symbols in the historic language of weather map plotters. *Bulletin of American Meteorological Society*, 100(12), 423–443. <https://doi.org/10.1175/BAMS-D-19-0071.1>
- Hübnová, I., Brabec, M., Malý, M., Dumitrescu, A., & Geletič, J. (2021). Terrain and its effects on fog occurrence. *Science of the Total Environment*, 768, 144359. <https://doi.org/10.1016/j.scitotenv.2020.144359>
- Imre K., Molnar A., Peterka A., Ferenczi Z., Horvath A., Weidinger T., & Gelencser A. (2019). Characterization of particle-droplet interactions in wintertime fog in Hungary: results of an intensive monitoring campaign. *8th International Conference on Fog, Fog Collection and Dew*, 14–19 July 2019, Taipei Taiwan. P-2-11: IFDA2019-168. <https://meetings.copernicus.org/ifa2019/>
- Jacobs, W., Nietosvaara, V., Bott, A., Bendix, J., Cermak, J., Michaelides, S., & Gulpepe, I. (Eds.). (2008). *Short range forecasting methods of fog, visibility and low clouds*. ESSEM COST Action 722 Final Report, Office for Official Publications of the European Communities: Luxembourg, 206 p. Publisher(s): EU Publications Office (OPOCE) <http://bookshop.europa.eu/uri?target=EUB:NOTICE:QSNA21451:EN:HTML>, ISBN/ISSN: 978-92-898-0005-1
- Jin, Y., Liu, Y., Liu, J., & Zhang, X. (2022). Energy balance closure problem over a tropical seasonal rainforest in Xishuangbanna, Southwest China: Role of latent heat flux. *Water*, 14(3), 395. <https://doi.org/10.3390/w14030395>
- Kivalov, S. N., Dušek, J., Czerný, R., Jocher, G., Pavelka, M., Fitzjarrald, D. R., Darenová, É., Šigut, L., & Kowalska, N. (2023). Addressing effects of environment on eddy-covariance flux estimates at a temperate sedge-grass marsh. *Boundary-Layer Meteorology*, 186, 217–250. <https://doi.org/10.1007/s10546-022-00755-0>
- Klemm, O., & Lin, N. (2016). What causes observed fog trends: Air quality or climate change? *Aerosol and Air Quality Research*, 16, 1131–1142. <https://doi.org/10.4209/aaqr.2015.05.0353>
- Klemm, O., Milford, C., Sutton, M. A., Spindler, G., & Van Putten, E. (2002). A climatology of leaf surface wetness. *Theoretical and Applied Climatology*, 71, 107–117. <https://doi.org/10.1007/s704-002-8211-5>
- Klemm, O., Wrzensiky, T., & Scheer, C. (2005). Fog water flux at a canopy top: Direct measurement versus one-dimensional model. *Atmospheric Environment*, 39, 5375–5386. <https://doi.org/10.1016/j.atmosenv.2005.05.041>
- Kljun, N., Calanca, P., Rotach, M. W., & Schmid, H. P. (2015). A simple two-dimensional parameterisation for flux footprint prediction (FFP). *Geoscientific Model Development*, 8(11), 3695–3713. <https://doi.org/10.5194/gmd-8-3695-2015>
- Kolláth, K., & Kolláth, Z. (2020). On the feasibility of using ceilometer backscatter profile as input data for skyglow simulation. *Journal of Quantitative Spectroscopy and Radiative Transfer*, 253, 107158. <https://doi.org/10.1016/j.jqsrt.2020.107158>
- Kumar, J., & Schmeller, G. (2022). Assessment of WRF planetary boundary layer (PBL) schemes in the simulation of Fog events over Hungary. *Időjárás*, 127(1), 1–22. <https://doi.org/10.28974/idojaras.2023.1.1>
- Kyrrouac, J., & Theisen, A. (2017). Biases of the MET Temperature and Relative Humidity Sensor (HMP45). *Report (No. DOE/SC-ARM-TR-192)*. DOE Office of Science Atmospheric Radiation Measurement, (ARM) Program (United States), 33 p. <https://doi.org/10.2172/1366737>
- Lee, H. B., Heo, J. H., & Sohn, E. H. (2021). Korean fog probability retrieval using remote sensing combined with machine-learning. *Giscience & Remote Sensing*, 58(8), 1434–1457. <https://doi.org/10.1080/15481603.2021.1995973>
- Li, M. N., Niu, S. J., Zhang, S. T., & Fei, D. D. (2015). Comparative study of turbulent characteristics between the fog day and haze day in Nanjing. *Acta Meteorologica Sinica*, 73, 593–608. <https://doi.org/10.11676/qxxb2015.032>
- Li, Z. H., Huang, J. P., Sun, B. Y., & Peng, H. (1999). Burst characteristics during the development of radiation fog. *Chinese Journal of Atmospheric Science*, 23, 623–631. <https://doi.org/10.3878/j.issn.1006-9895.1999.05.13>
- Liebenthal, C., & Foken, T. (2007). Evaluation of six parameterization approaches for the ground heat flux. *Theoretical and Applied ClimatolOgy*, 88, 43–56. <https://doi.org/10.1007/s00704-005-0234-0>
- Lin, D., Katurji, M., Revell, L. E., Khan, B., Osborne, N., Soltanzadeh, I., & Kremser, S. (2022). Fog type classification using a modified Richardson number for Christchurch, New Zealand. *International Journal of Climatology*, 43(1), 314–330. <https://doi.org/10.1002/joc.7761>
- Liu, Q., Wu, B., Wang, Z., & Hao, T. (2020). Fog droplet size distribution and the interaction between fog droplets and fine particles during dense fog in Tianjin, China. *Atmosphere*, 11, 258. <https://doi.org/10.3390/atmos11030258>
- Matus, V., Eso, E., Teli, S. R., Perez-Jimenez, R., & Zvanovec, S. (2020). Experimentally derived feasibility of optical camera communications under turbulence and fog conditions. *Sensors*, 20(3), 757. <https://doi.org/10.3390/s20030757>
- Mauder, M., & Foken, T. (2015). *Documentation and Instruction Manual of the Eddy-Covariance Software Package TK3 (update)*. Universität Bayreuth, Abt. Mikrometeorologie, 68 p. ISSN 1614–8924.
- Menut, L., Mailler, S., Dupont, J. C., Haeffelin, M., & Elias, T. (2014). Predictability of the meteorological conditions favourable to radiative fog formation during the 2011 ParisFog campaign. *Boundary-Layer Meteorology*, 150(2), 277–297. <https://doi.org/10.1007/s10546-013-9875-1>

- Meyer, M. B., & Lala, G. G. (1990). Climatological aspects of radiation fog occurrence at Albany, New York. *Journal of Climate*, 3(5), 577–586. [https://doi.org/10.1175/1520-0442\(1990\)003%3c0577:CAORFO%3e2.0.CO;2](https://doi.org/10.1175/1520-0442(1990)003%3c0577:CAORFO%3e2.0.CO;2)
- Miclea, R.-C., Dughir, C., Alexa, F., Sandru, F., & Silea, I. (2020). Laser and LIDAR in a system for visibility distance estimation in fog conditions. *Sensors*, 20(21), 6322. <https://doi.org/10.3390/s20216322>
- Möller, D. (2008). On the history of the scientific exploration of fog, dew, rain and other atmospheric water. *Die Erde*, 139(1–2), 11–44.
- Nakanishi, M. (2000). Large-eddy simulation of radiation fog. *Boundary-Layer Meteorology*, 94(3), 461–493. <https://doi.org/10.1023/A:1002490423389>
- Nowak, D., Ruffieux, D., Agnew, J. L., & Vuilleumier, L. (2008). Detection of fog and low cloud boundaries with ground-based remote sensing systems. *Journal of Atmospheric and Ocean Technology*, 25, 1357–1368. <https://doi.org/10.1175/2007JTECHA950.1>
- Ovesnik, D., Turán, J., Misencik, P., Bitó, J., & Csurgai-Horváth, L. (2012). Fog density measuring system. *Acta Electrotechnica Et Informatica*, 12(2), 67–71. <https://doi.org/10.2478/v10198-012-0021-767>
- Panofsky, H. A., & Dutton, J. A. (1984). *Atmospheric turbulence. Models and methods for engineering applications*. Wiley.
- Pauli, E., Andersen, H., Bendix, J., Cermak, J., & Egli, S. (2020). Determinants of fog and low stratus occurrence in continental central Europe—a quantitative satellite-based evaluation. *Journal of Hydrology*, 591, 125451. <https://doi.org/10.1016/j.jhydrol.2020.125451>
- Peterka, A., Thompson, G., & Geresdi, I. (2024). Numerical prediction of fog: A novel parameterization for droplet formation. *Quarterly Journal of Royal Meteorological Society*. <https://doi.org/10.1002/qj.4704>
- Pithani, P., Ghude, S. D., Jenamani, R. K., Biswas, M., Naidu, C. V., Debnath, S., Kulkarni, R., Dhangar, N. G., Jena, C., Hazra, A., Phani, R., Mukhopadhyay, P., Prabhakaran, T., Nanjundiah, R. S., & Rajeevan, M. (2020). Real-time forecast of dense fog events over Delhi: The performance of the WRF model during the WiFEX field campaign. *Weather and Forecasting*, 35(2), 739–756. <https://doi.org/10.1175/WAF-D-19-0104.1>
- Price, J. D. (2019). On the formation and development of radiation fog: An observational study. *Boundary-Layer Meteorology*, 172(2), 167–197. <https://doi.org/10.1007/s10546-019-00444-5>
- Price, J. D., Lane, S., Boutle, I. A., Smith, D. K. E., Bergot, T., Lac, C., Duconge, L., McGregor, J., Kerr-Munslow, A., Pickering, M., & Clark, R. (2018). LANFEX: A field and modeling study to improve our understanding and forecasting of radiation fog and Large-Eddy simulation of radiation fog. *Bulletin of American Meteorological Society*, 99(10), 2061–2077. <https://doi.org/10.1175/BAMS-D-16-0299.1>
- Pu, Z., Chachere, C. N., Hoch, S. W., Pardyjak, E., & Gultepe, I. (2016). Numerical prediction of cold season fog events over complex terrain: The performance of the WRF model during MATERHORN-fog and early evaluation. *Pure and Applied Geophysics*, 173(9), 3165–3186. <https://doi.org/10.1007/s00024-016-1375-z>
- Rahman, M. M., Zhang, W., & Wang, K. (2019). Assessment on surface energy imbalance and energy partitioning using ground and satellite data over a semi-arid agricultural region in north China. *Agricultural Water Management*, 213, 245–259. <https://doi.org/10.1016/j.agwat.2018.10.032>
- Shen, C., Zhao, C., Ma, N., Tao, J., Zhao, G., Yu, Y., & Kuang, Y. (2018). Method to estimate water vapor supersaturation in the ambient activation process using aerosol and droplet measurement data. *Journal of Geophysical Research: Atmospheres*, 123(18), 10606–10619. <https://doi.org/10.1029/2018JD028315>
- Smith, D. K. E., Renfrew, I. A., Dorling, S. R., Price, J. D., & Boutle, I. A. (2021). Sub-km scale numerical weather prediction model simulations of radiation fog. *Quarterly Journal of Royal Meteorological Society*, 147, 746–763. <https://doi.org/10.1002/qj.3943>
- Spirig, R., Vogt, R., Larsen, J. A., Feigenwinter, C., Wicki, A., Franceschi, J., Parlow, E., Adler, B., Kalthoff, N., Cermak, J., & Andersen, H. (2019). Probing the fog life cycles in the Namib Desert. *Bulletin of American Meteorological Society*, 100(12), 2491–2507. <https://doi.org/10.1175/BAMS-D-18-0142.1>
- Szintai, B., Bazile, E., & Seity, Y. (2019). Improving wintertime low level cloud forecasts in a high-resolution numerical weather prediction model. *Időjárás*, 123(2), 183–202. <https://doi.org/10.28974/idojaras.2019.2.4>
- Tardif, R., & Rasmussen, R. M. (2007). Event-based climatology and typology of fog in the New York City region. *Journal of Applied Meteorology and Climatology*, 46(8), 1141–1168. <https://doi.org/10.1175/JAM2516.1>
- Temimi, M., Fonseca, R. M., Nelli, N. R., Valappil, V. K., Weston, M. J., Thota, M. S., Wehbe, Y., & Yousef, L. (2020). On the analysis of ground-based microwave radiometer data during fog conditions. *Atmospheric Research*, 231, 104652. <https://doi.org/10.1016/j.atmosres.2019.104652>
- Tuba, Z., & Bottyán, Zs. (2018). Fuzzy logic-based analogue forecasting and hybrid modelling of horizontal visibility. *Meteorology and Atmospheric Physics*, 130, 265–277. <https://doi.org/10.1007/s00703-017-0513-1>
- Varga-Balogh, A., Leelőssy, Á., Lagzi, I., & Mészáros, R. (2020). Time-dependent downscaling of PM predictions from CAMS air quality models to urban monitoring sites in Budapest. *Atmosphere*, 11, 669. <https://doi.org/10.3390/atmos1106066>
- Wang, S., Fernando, H. J. S., Dorman, C., Creegan, E., Krishnamurthy, R., Wainwright, C., Wagh, S., & Yamaguchi, R. (2021). Analysis of coastal fog from a ship during the C-FOG Campaign. *Boundary-Layer Meteorology*, 181, 365–393. <https://doi.org/10.1007/s10546-021-00667-5>
- Weidinger, T., Varga, A., Breuer, H., Gyongyosi, A.Z., Krámer, T., Reháč, A., Szilágyi, M., Torma, P., Geresdi, I., Peterka, A., Kardos, P., Bottyan, Zs., Horváth, Á., Pappné Ferenczi, Z., Lázár, I., & Imre, K. (2021b). An experimental and numerical study of foggy situations in the Pannonian basin during winter cold-air pool events (Hungarian Fog Experiment 2018–20). *103rd AMS Annual Meeting*. https://doi.org/10.1175/AMS_Boundary_Layer_Symp_2023.pdf
- Weidinger, T., Gyöngyösi, A. Z., Gandhi, A., Tordai, Á., Krámer, T., Torma, P., Reháč, A., Szilágyi, M., Horváth, Á., Horváth, Gy., Bottyán, Zs., Cséplő, A., Lázár, I., Imre, K., Kardos, P., &

- Geresdi, I. (2021a). Micrometeorological fog experiments in Budapest and in Sió Valley near Lake Balaton (2018–2021). *EMS Annual Meeting Abstracts*, 18, 304. <https://doi.org/10.5194/ems2021-304>
- Wilson, K., Goldstein, A., Falge, E., Aubinet, M., Baldocchi, D., Berbigier, P., Bernhofer, C., Ceulemans, R., Dolman, H., Field, C., Grelle, A., Ibrom, A., Law, B. E., Kowalski, A., Meyers, T., Moncrieff, J., Monson, R., Oechel, W., Tenhunen, J., ... Verma, S. (2002). Energy balance closure at FLUXNET sites. *Agricultural and Forest Meteorology*, 113(1–4), 223–243. [https://doi.org/10.1016/S0168-1923\(02\)00109-0](https://doi.org/10.1016/S0168-1923(02)00109-0)
- Zhou, B., & Ferrier, B. S. (2008). Asymptotic analysis of equilibrium in radiation fog. *Journal of Applied Meteorology and Climatology*, 47(6), 1704–1722. <https://doi.org/10.1175/2007JAMC1685.1>
- Zoldos, M., & Jurkovic, M. (2016). Fog event climatology for Zagreb Airport. *Hrvatski Meteorološki Časopis/croatian Meteorological Journal*, 51, 13–26.

(Received June 26, 2023, revised April 21, 2024, accepted April 29, 2024)